ESA – AO/1-5467/07/NL/HE

A SPONTANEOUS RAYLEIGH-BRILLOUIN SCATTERING EXPERIMENT FOR THE CHARACTERIZATION OF ATMOSPHERIC LIDAR BACKSCATTER

Technical Note 4, Part 3

version 5; 11-Dec-2009

RB scattering uncertainty effects on ADM-Aeolus winds

Jos de Kloe and Ad Stoffelen
KNMI, Royal Netherlands Meteorological Institute, de Bilt, Netherlands

Contents

List of Abbreviations and Symbols

ADM	Atmospheric Dynamics Mission
CRBS	Coherent Rayleigh-Brillouin Scattering
E2S	End-to-End Simulator (instrument simulator)
ESA	European Space Agency
FFT	Fast Fourier Transform
FP	Fabry-Pérot
L2b	Aeolus Level 2b product (wind profiles)
LOS	Line-of-Sight
NWP	Numerical Weather Prediction
PDF	Probability Density Function
RB	Rayleigh-Brillouin
rbs	fitting program to the updated Tenti code; provided by Willem van de Water
SRP	Spontaneous Rayleigh-Brillouin
SRBS	Spontaneous Rayleigh-Brillouin Scattering
TN	Technical Note
USR	Useful Spectral Range
VU	Free University of Amsterdam…..
A	Integrated signal on FP spectrometer A (direct channel, in [counts])
B	Integrated signal on FP spectrometer B (reflected channel, [counts])
c	speed of light in vacuum in [m/s]
R	Response of the combined dual edge spectrometer detection system
λ	Laser wavelength (in [m])
$\delta\lambda$	Doppler shift (in [m])
ν_{LOS}	Component if the local windspeed projected on the line-of-sight of the lidar system

1 Introduction

As described and reported in earlier Technical Notes (TNs) for this study, the molecular scattering functions of light in air are not just Gaussian profiles, depending only on the Brownian motion probability density function (PDF) of the gas mixture. In fact, all collisional properties of the molecular gas contribute to the scattering profile. In particular acoustic phenomena, known to produce the characteristic Brillouin side-wings on the molecular backscatter profile have a strong effect. The ESA study, ILIAD [R3], showed that Brillouin scattering has an important contribution to atmospheric backscatter from Lidars. ILIAD showed that the neglecting of Brillouin scattering might result in errors in the Doppler wind measurements by ESA's Lidar mission, ADM-Aeolus, of up to 10% in several cases.
Earlier TNs from this study have shown that the Brillouin effect is best described by the so-called Tenti S6 model. In TN4_part1, the Tenti S6 and S7 models were validated against new experimental measurements of spontaneous and coherent Rayleigh-Brillouin scattering (RBS) in air for a set of pressures and temperatures representative for the Earth's atmosphere. In light of this Tenti model validation, the implications of the Brillouin effect on the ESA ADM-Aeolus mission are investigated in this TN.

ADM-Aeolus uses a priori information on the molecular motion PDF to determine shifts in this distribution by the mean atmospheric motion, or wind. This is done by placing two Fabry-Pérot (FP) interferometers, each centered at one side of the molecular motion PDF, and measuring the normalized difference in signal detected by the two FPs. As the molecular motion PDF is shifted by the local atmospheric motion (wind), one of the FPs detects an increasing signal, while the other FP detects a descreasing signal (Figure 1).

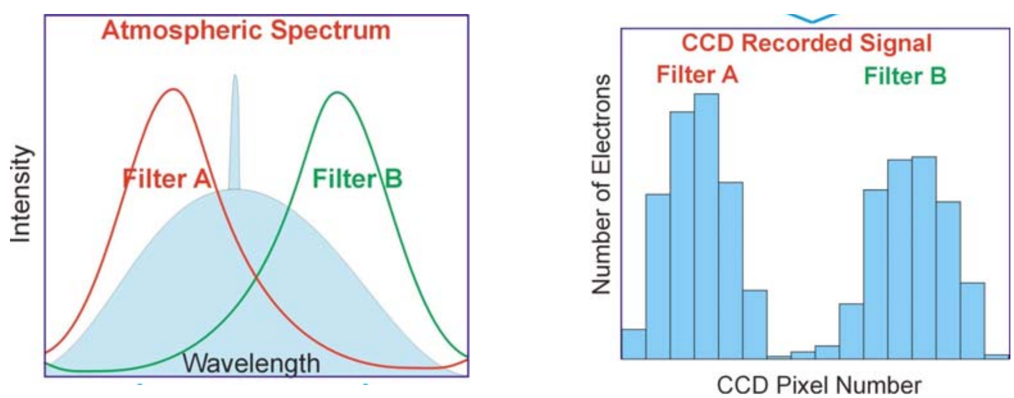

Figure 1: Detection of the Doppler shifted backscattered laser light (left panel) on the Aeolus Dual Fabry-Pérot detectors. CCD: Charge-Coupled Device. Note that the varying signal for the columns for filter A (or B) are not caused by a wavelength dependent transmission (as would be suggested by comparing with the spectrum in the left panel), but are a consequence of the circular shape of the spot in which the output signal of Filter A (or B) is projected onto the ACCD.

Following this effect, a response, which is the normalized difference in the FP signals, is defined. The response is (almost) proportional to the measured wind. The ADM-Aeolus detectors are time-gated, allowing the detection of a wind profile from 24 atmospheric layers throughout the atmosphere. In addition, the ADM-Aeolus instrument also contains a Fizeau spectrometer to resolve the Mie scattered light. A schematic view of the spectrometers is given in Figure 2. It is important to note here that the light is first transferred to the Fizeau spectrometer (Mie signal detector). The light reflected from this Fizeau spectrometer is transferred to the first (direct) FP spectrometer. The remaining light, reflected from this first FP spectrometer, is finally transferred to the second (indirect) FP spectrometer. For more details on the Aeolus mission and measurement concept, see [R1].

In the case that the exact shape of the Rayleigh-Brillouin (RB) molecular motion PDF is not precisely known, the interpretation of this normalized signal difference (response) as an integral shift of the RB spectral shape becomes uncertain.
In this TN, the effect of the uncertainty in the temperature and pressure dependent shapes of RBS on the expected quality of the ADM-Aeolus wind profiles that will be retrieved by the L2b processing software is estimated. This is done by using the measured RB line shapes for a set of temperatures and pressures from the Spontaneous Rayleigh-Brillouin Scattering (SRBS) experiments at the VU (Free University of Amsterdam) and the updated version of the Tenti S6 code developed at the University of Nijmegen and Eindhoven (described in TN4 part 1 and 2).

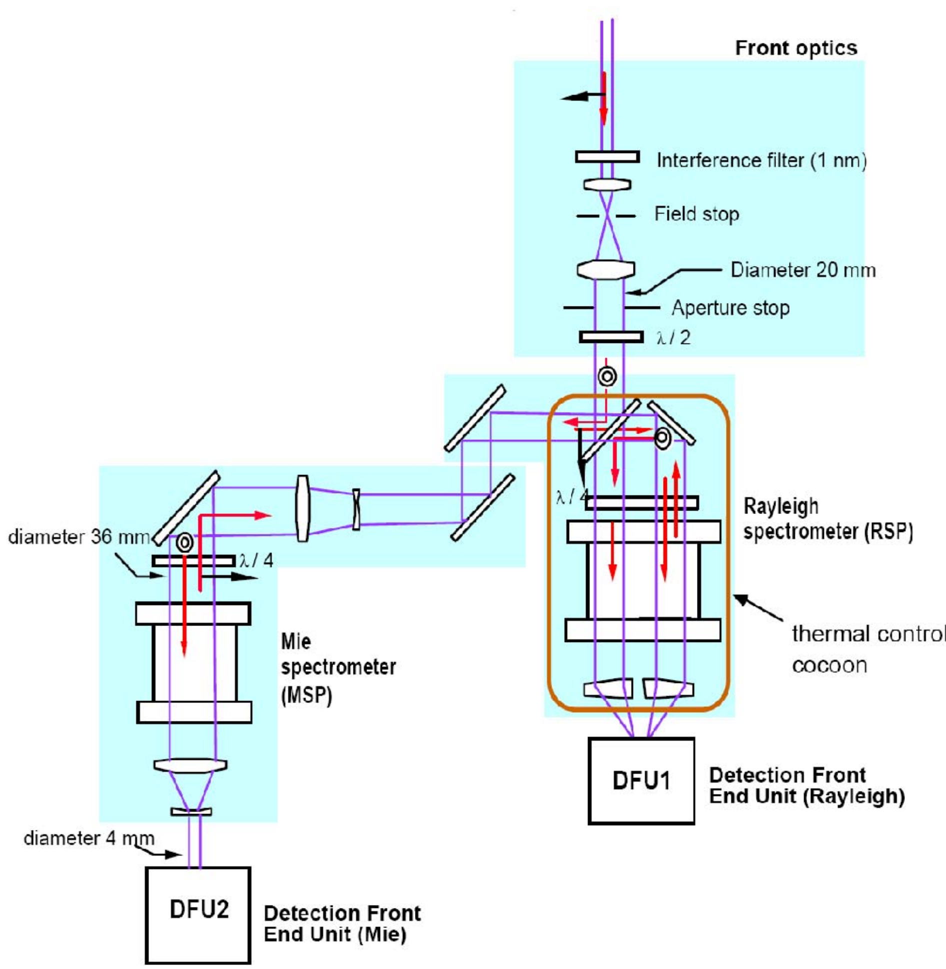

Figure 2: Schematic view of the Spectrometers used by ADM-Aeolus

The SRBS measurements, as performed with the novel UV-laser RB-spectrometer developed at VU, are described in section 3. The effect of the measured RBS line shapes on the Aeolus wind retrieval is presented in section 7. The measurements by the Coherent Rayleigh Brillouin Scattering (CRBS) experiment in Nijmegen (described in TN3 part 2) were not used here because the SRBS measurements are more representative of the laser and the atmospheric conditions that will be encountered by Aeolus. However, it should be noted that the CRBS results are consistent with the SRBS results when compared to the Tenti S6 model, as concluded in TN4 part 1.

At first a simple approach was followed, trying to convert the residuals between observation and theory from the VU to the ADM measurement geometry. In this approach the effect of convolution by the VU FP instrument function and the difference in wavelength was neglected, and the frequency axis was scaled by a factor sqrt(2) to account for the change in geometry.

After discussions within the team it was felt this was not the right approach. The VU FP instrument function, the difference in wavelength and in geometry needed to be taken into account in a more systematic way. A relatively easy to implement solution was to use deconvolution of the data by the instrument function, and use the x parameter to scale the shape from one wavelength and geometry to the other. This new approach is the one described in the following sections.

This TN is organized in the following manner:

- First the response functions of the Fabry-Pérot systems used at the VU experiment, and the system used in the ADM-Aeolus satellite are described (see section 2);
- Then a number of SRBS experiments for dry Air performed at the VU have been selected (see section 3);
- The measured spectra are then deconvolved to remove the effect of the Airy transmission function of the Fabry-Pérot spectrometer used in the experiment (see section 4);
- Using the measured temperature, pressure and geometry, the theoretical RB spectral shapes are calculated using the Tenti S6 and S7 models and, as a reference, also a Gaussian model. For these calculations, the new Tenti code presented in TN4 part 1 was used. Then the differences between modelled line shapes and the experiment (the residuals) are converted from the VU to the Aeolus geometry and wavelength (see section 5);
- These rescaled residuals are added to the Tenti model calculated RBS spectral shape for the ADM-Aeolus wavelength and geometry. The spectra are then Doppler-shifted to simulate a set of LOS wind velocities as measured by ADM-Aeolus.. Then the original (Tenti) and modified (Tenti + measurement residual) shapes are used to estimate the response as seen by the Aeolus Fabry-Pérot spectrometer for the above mentioned series of Line-of-Sight (LOS) wind velocities. The responses are then used to calculate the LOS wind deviations (see section 6);
- Finally, the results are summarized, some conclusions and recommendations are given and the application to the Aeolus L2B processing stage is discussed (see section 7).

2 Tenti Spectral Shapes

Both the experimental setup at the VU, and the ADM-Aeolus satellite, use Fabry-Pérot interferometers to detect the Rayleigh scattered light. However, apart from the different characteristics of the spectrometers themselves (as listed in Table 1), the ADM-Aeolus system also has a very different setup because the light is transferred from one spectrometer to the other (see Figure 2). This implies that the 3 spectrometers used in the ADM-Aeolus system all leave their signature in the detected spectrum once the light reaches the 3rd and last spectrometer.

	FSR	FWHM	peak transmission
VU FP	232 MHz	7440 MHz	1. (normalised)
ADM Direct FP	1666 MHz	10950 MHz	0.68
ADM Reflected FP	1666 MHz	10950 MHz	0.61
ADM Fizeau	2150 MHz	184 MHz	0.60
Some ADM specific settings:			
ADM FP spectral spacing		ADM Fizeau USR	
5475.1 MHz or 2.3 pm		1502 MHz	

Table 1: Some properties of the Fabry-Pérot and Fizeau spectrometers

The response functions of the Fabry-Pérot systems used at the VU experiment are modelled using an Airy instrument function (see section 2.1.3 of TN3 part 1) with FSR and FWHM as specified in Table 1. No additional Gaussian instrument error function has been applied (Figure 3). Note that this same response function is used in the deconvolution of all experiments described below. There has been some discussion on the validity of this approach. The perfect Airy function does not fit the height of the different measured FP instrument modes very well. This is solved by rescaling each mode again to a top value of one. However, this rescaling combined with measurement noise might introduce small deviations in the shape of the transmission peak if many modes are accumulated to obtain a better SNR. This might be investigated in more detail in a follow-up study, but in view of the available time of the current task it is not possible within this project. Therefore the following chapters assume a perfect Airy function describes the instrument function to sufficient detail.

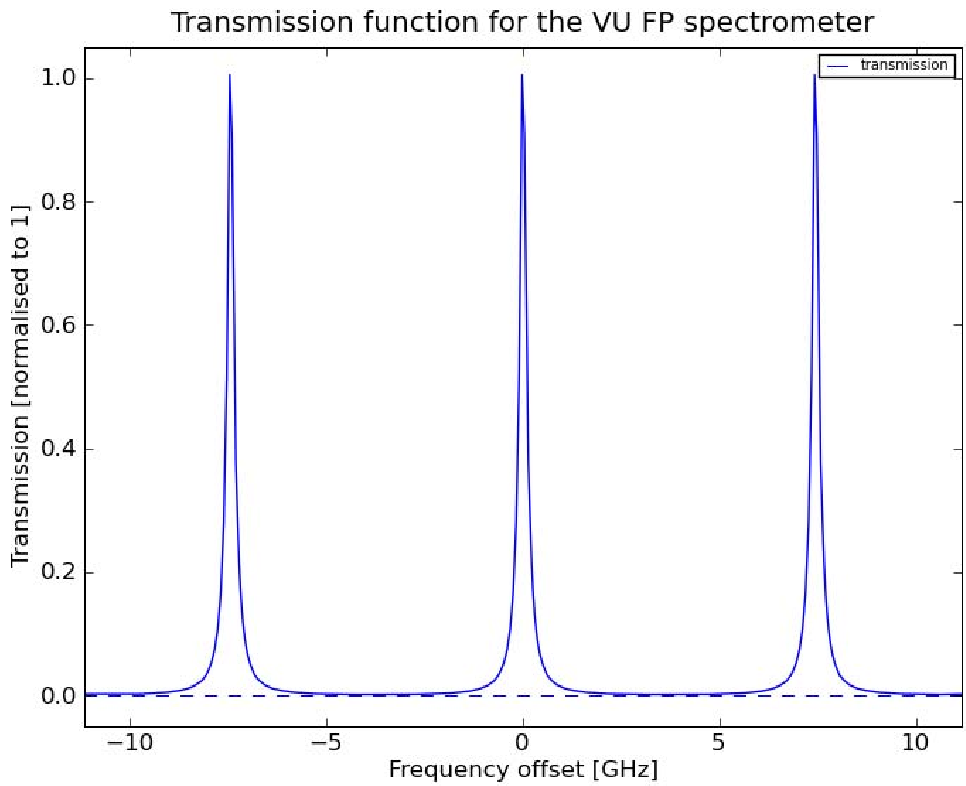

Figure 3: Airy function used to model the transmission of the VU FP spectrometer.

The system used in the ADM-Aeolus satellite is far more complicated. The response of the FP spectrometer of ADM-Aeolus Doppler Wind Lidar receiver has been modelled by taking a copy of the implementation in the End-to-End Simulator (E2S) provided by ESA, and converting the Matlab code into Fortran (see [R2] section 7.9 and 7.10).

This includes the following steps:

- Calculate the reflection on the Fizeau plate, since this will be used as input for the Fabry-Pérot spectrometer. This reflection depends on the location at the Fizeau plate on which the reflection occurs. At each location the transmission is assumed to have the shape of an Airy function, and the reflection is taken to be one minus the transmission.
- Since the FP transmission should not depend on the location of the light spot, the Fizeau reflection is now averaged over the whole Fizeau plate for each simulated frequency. This simplifies the calculations significantly, since otherwise some kind of ray-tracing procedure would be needed to proceed with the simulation. This reflection is illustrated in figure 4 by the red wavy line just below the level of 1. The waves are caused by the periodicity of the Airy function, which causes a gradual shift in the number of periods that fit onto the Fizeau plate.
- The signal reflected on the Fizeau plate then enters the direct channel of the FP spectrometer, for which the transmission again is modelled as an Airy function (but with much broader Useful Spectral Range (USR) and FSR, see Table 1). Note that the USR is a specific Fizeau spectrometer property, since for that system the spectral

range is determined by the size and geometry of the Fizeau plate, and not scanned as is done for the VU FP system. The transmission is given as the blue line in figure 4, and the wiggly modulated dotted line around it depicts the combined Fizeau reflection and FP-direct channel transmission.

- The reflection from the first FP spectrometer is again taken to be one minus the transmission, and is shown as the green line in figure 4.
- Finally the transmission for the reflected FP channel also is modelled using an Airy function (see the light blue line in figure 4). The wiggly modulated line around it, going to zero close to 1.1 pm is the combined Fizeau reflection, direct-FP channel reflection and reflected-FP channel transmission.

Note here that all these lines have been scaled such that their maximum is at 1.

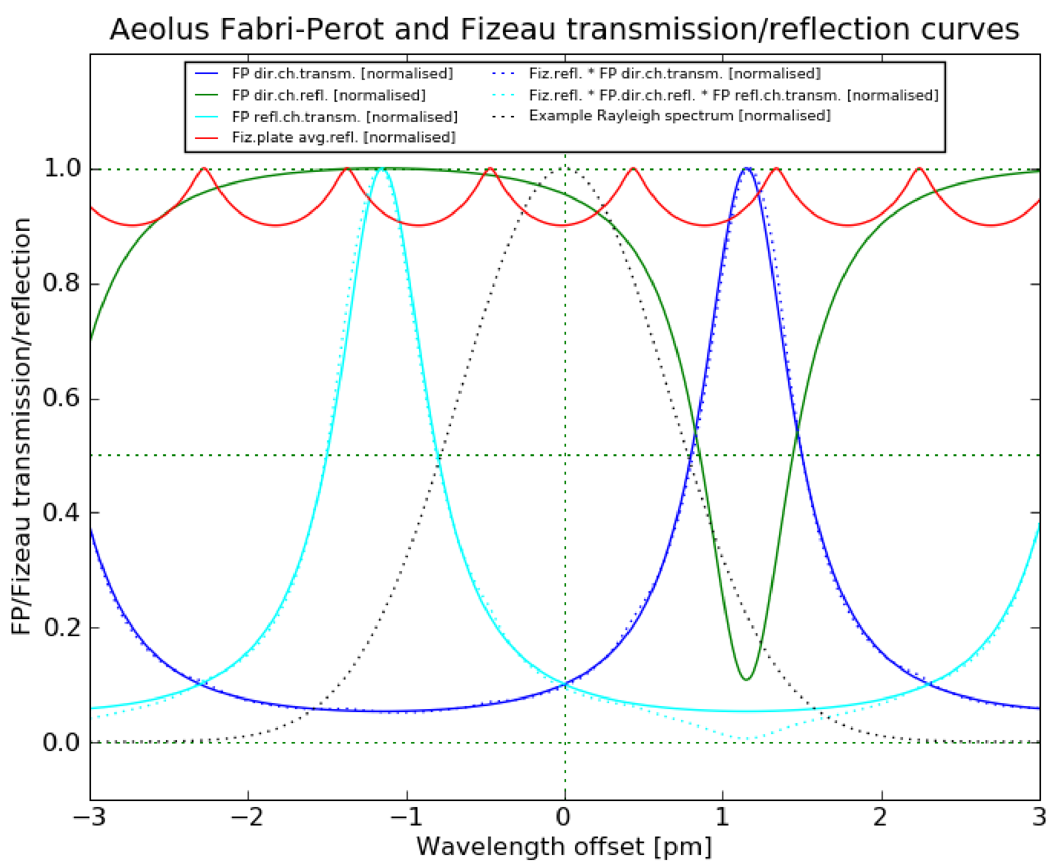

Figure 4: Simulated transmission and reflection on the active optical components used by the ADM-Aeolus detection system.

3 Selected experiments

A number of SRBS experiments for dry Air performed at the VU have been selected for this evaluation. Pressures range between 300 hPa and 1040 hPa, and have been chosen since these are realistic values that can occur in the real atmosphere as well.

There is not much temperature variation, since all these experiments where performed at room temperature. The gas mixture used to represent air was 79% pure N_2 and 21% pure O_2, so not real air.

For convenience of referencing, the 9 selected experiments have been assigned the numbers 1 up to 9. An overview of the pressures and temperatures for the selected experiments is given in Table 2 below.

Reference number	Pressure [hPa]	Tempera-ture [C]	Filename
1	300	24.8	Air_300mbar_scan20090625_06_7440MHz_res23.25MHz see TN3p1, section 5,1, case 1
2	503	25.7	Air_500mbar_scan20090617_02_7440MHz_res18.6MHz see TN3p1, section 5.2, case 1
3	504	24.8	Air_500mbar_scan20090625_07_7440MHz_res37.2MHz see TN3p1, section 5.2, case 2
4	500	23.5	Air_500mbar_mie_scan20091001_05_n_7440MHz_res25MHz see TN3p1, section 5.2, case 3
5	725	25.7	Air_725mbar_scan20090617_01_7440MHz_res37.2MHz see TN3p1, section 5.3, case 1
6	1040	23.5	Air_1000mbar_scan20090615_07_7440MHz_res18.6MHz see TN3p1, section 5.4, case 1
7	1040	22.9	Air_1000mbar_scan20090616_01_n_7440MHz_res46.5MHz see TN3p1, section 5.4, case 2
8	1040	25.0	Air_1000mbar_scan20090626_01_n_7440MHz_res37.2MHz see TN3p1, section 5.4, case 3
9	1008	24.0	Air_1000mbar_scan20090925_03_n_7440MHz_res25MHz see TN3p1, section 5.4, case 4

Table 2: Overview of the parameters for the selected experiments.

It has to be noted that experiment 4 was clearly contaminated by a Mie peak, and has been added on purpose, to study this effect and allow comparison with the other more clean cases.

4 Deconvolution of the experimental data

The measured spectra are a convolution of the real spectral shape (modelled by the Tenti model) and a FP transmission function. To study the difference between Tenti model and experiments the measured spectra thus need to be deconvolved to remove the effect on the spectrum of the Airy transmission function of the Fabry-Pérot spectrometer used in the experiment. This deconvoluted spectrum is subsequently used to rescale to the different Aeolus geometry and wavelength (see next section). Such rescaling cannot be done on the actual measured signal because of the large difference in the properties of the spectrometers used for both cases (see Table 1) and because of the large effect of the FP properties on the measurements.

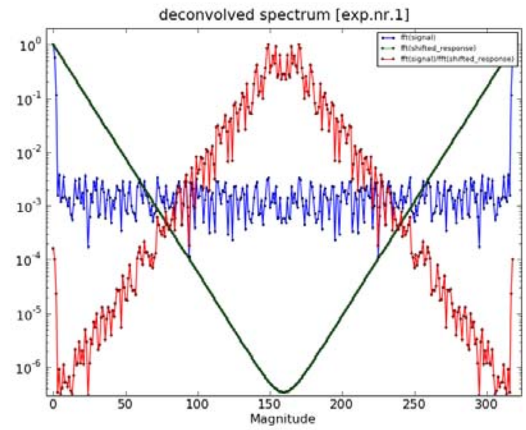

Figure 5: Illustration of deconvolution without filtering (see text).

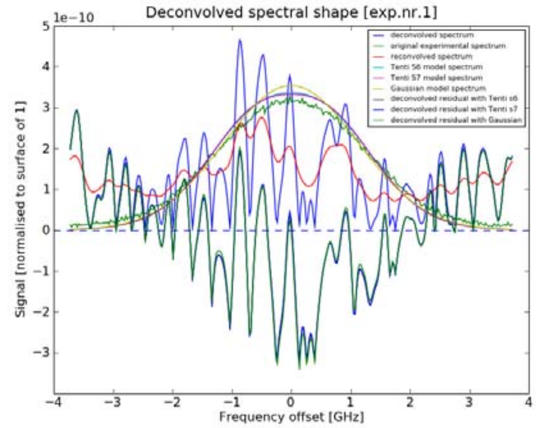

Figure 6: The resulting not well-behaved deconvoluted spectra (see text).

In theory deconvolution is a simple division in the Fourier domain, i.e., calculate the Fourier transformations of the spectrum and the instrument function, divide one by the other, and do an inverse Fourier transform.

However this might work well for nicely defined theoretical functions, when applied to noisy data, this procedure fails miserably. It usually strongly amplifies the Fourier terms that correspond to the higher frequencies, and in the end, the deconvolved signal seems to contain only noise. This is illustrated in Figures 5 and 6. In Figure 5 the blue line indicates the Fourier transformed spectrum, the black line indicates the Fourier transformed transmission function, and the red line indicates the division between the two. Clearly the higher frequencies between 100 and 200 become dominant. The resulting deconvolved spectrum as shown in Figure 6 clearly cannot be used for further analysis. The meaning of the different lines in this figure is explained in detail in the next section.

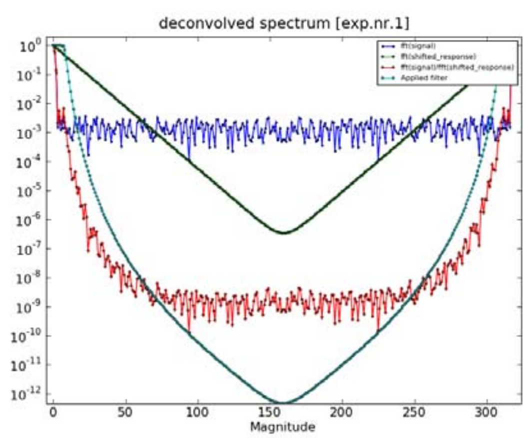

Figure 7: Illustration of the effect of filtering on the deconvolution

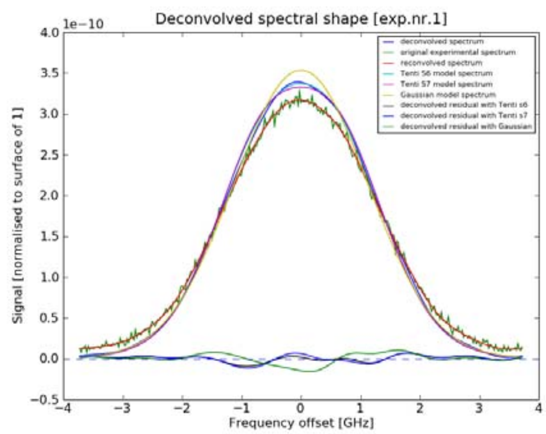

Figure 8: The resulting deconvoluted spectra.

This can be solved by applying filtering in the Fourier domain, which attenuates the higher

frequencies and does not alter the lower frequencies too much.
For the current study a Butterworth filter has been applied on the Fourier terms, just before doing the inverse Fourier transform. The filter settings have been found by trial and error, and eventually the settings used are a filter order of 9, and a -3dB location of 0.025 (this is after rescaling the Fourier domain to the range 0 - 1.0). When using these settings, no additional smoothing was needed to remove noise. The shape of the filter transmission is illustrated in Figure 7 as the light-blue line. The effect is clearly visible on the red curve, which now strongly suppresses all high frequency terms. The resulting deconvoluted spectra now look very clean and should be suitable for further analysis (Figure 8).
Finally, please note that the offset correction that has been implemented in the rbs fitting program (updated Tenti code by Willem van de Water) has not been applied here. This sometimes may lead to problems, which is further discussed in the conclusions (section 7).

5 Determination and rescaling of the residuals

The SRB measurements resulted in a residual, i.e., the difference between expected (Tenti modelled) and measured spectral shapes. This residual presents the remaining uncertainty after the measurements and here we attempt to compute its effect in the Aeolus geometry. An overview of the steps taken for each of the 9 experimental cases is given in the flow-diagram presented in Figure 9. A stepwise description of the implemented method is:

- Step a: Using the measured temperature, pressure and the geometry and wavelength of the VU experiment (365 nm, 90^{o} scattering), the expected spectral shapes are calculated using the Tenti S6 and S7 models and, as a reference, also a Gaussian model. This is done by running the rbs program provided by Willem van de Water.
- Step b: the y-parameter (reduced wavelength) is retrieved from the outputs of the fit program as has been run in step a.
- Step c: then the rbs program is run many times in a loop to allow finding a pair of T, p values for the ADM-Aeolus geometry that result in the same y-value as was retrieved in step b (typically it runs about 250 times). This is needed to ensure the spectrum has a comparable shape for both geometries, which may have an influence on the shape of the residual. For the first experiment at first the temperature was scanned manually, and a value of -50 °C was found to give a very close match of y-parameter. Then, the pressure was scanned in an automated way. This has less influence on the y-parameter than the temperature, but still it was possible to adjust the y-parameter to the slightly varying temperatures in the experimental VU setup, by only adjusting the pressure. The temperature and pressure values found are reported in Table 3.
- Step d: the VU Fabry-Pérot instrument transmission function is calculated, assuming it can be modelled by an Airy function (see sections 2 and 7 for some discussion on this assumption).
- Step e: the x-parameter array (reduced frequency), the actual frequency array and the measured data from the VU experiment are retrieved from the output files of the rbs program as was run in step a.
- Step f: the measured data is deconvolved using the instrument function calculated in step d, and using the method described in section 4 above.
- Step g: the deconvolved data is convolved again with the mentioned instrument function to verify the procedure does not introduce too severe loss of information content.
- Step h: retrieve the theoretical Tenti spectra (Gaussian, S6 and S7) from the outputs of the rbs program, as was run in step a.
- Step i: combine the theoretical spectra and the deconvolved data into the residual curves (i.e., the difference between deconvoluted experiment and theory), and calculate the asymmetry for these curves. The results of this procedure are displayed in Figures 10 to 18. These figures show in the upper panel the measured spectrum (green line), the deconvolved spectrum (blue line), the reconvolved spectrum (red line), the model

spectra (Tenti S6, light blue line, Tenti S7, purple line, Gaussian, yellow line), and the residuals in the lower panel (for Tenti S6, blue line, Tenti S7, green line, Gaussian, red line). Note that the y-axis scaling was determined by calculating the surface below the spectrum, and setting it to a value of 1. In this part this was done using a frequency in Hz, rather than in GHz, which explains the difference in y-axis scale of the plots presented e.g. in TN4 part1. To check the consistency of the deconvolution procedure, the deconvoluted spectrum has been convolved again with the instrument function (see step g) and overplotted in this figure. This clearly shows any problems in the deconvolution that might occur. A deconvolution that has some clear problems is for example the one for experiment 4, see Figure 13. For this case the deconvolved spectrum does not seem to go to zero for frequencies with larger offset. This may be related to the presence of Mie contamination in this experiment, or to the fact that we did not take the offset (deviation from the zero level) in the data into account.

- Step j: run the rbs program using the temperature and pressure estimated for ADM-Aeolus in step c above, and the geometry and wavelength of ADM-Aeolus (355 nm, 180^{o} scattering angle), and calculate the expected spectral shapes using the Tenti S6 and S7 models, and as reference also for the Gaussian model.
- Step k: retrieve the x-parameter array (reduced frequency), the frequency array, and the theoretical Tenti spectra (Gaussian, S6 and S7) from the outputs of the rbs program, as was run in step j.
- Step l: resample the deconvoluted residuals (calculated in step i), from the x-array retrieved in step e, onto the x-array retrieved in step k. Undefined parts of the range are set to zero.
- Step m: translate the x-array to frequency for the ADM-Aeolus geometry and add the resampled deconvolved residual (for Tenti S6 or Tenti S7) to the theoretical Tenti spectrum for the ADM-Aeolus geometry (for Tenti S6 or Tenti S7). For the Gaussian residual a slightly different approach was chosen, to enable comparison with the earlier results presented in the ILIAD report [R3]. In this case the Tenti S6 spectral shape was taken as “truth” and then the Gaussian residual was added to that.

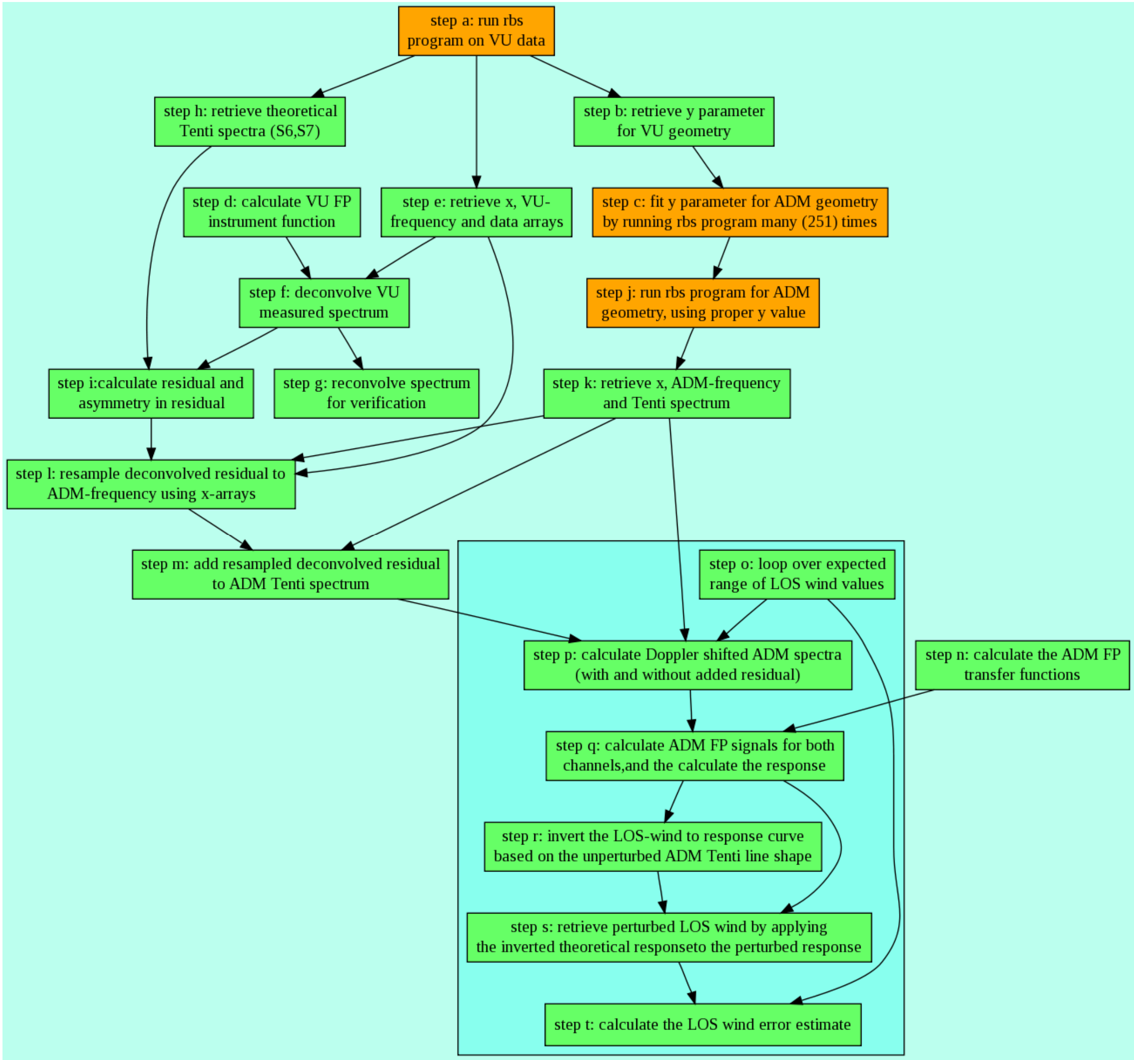

Figure 9: Flow-diagram of the steps needed to estimate the expected uncertainty in the LOS wind due to the uncertainty (residual) in the spectral shape.

	VU-geometry and wavelength			ADM_Aeolus-geometry and wavelength		
	scattering angle [degrees]	wavelength [nm]		scattering angle [degrees]	wavelength [nm]	
	90.0	366		180.0	355	
Reference number	Pressure [hPa]	Temperature [C]	y-parameter value	Pressure [hPa]	Temperature [C]	y-parameter value
1	300	24.8	0.1628	300.4	-50.0	0.16282
2	503	25.7	0.27198	501.8	-50.0	0.27197
3	504	24.8	0.27351	504.6	-50.0	0.27349
4	500	23.5	0.27285	503.4	-50.0	0.27284
5	725	25.7	0.39202	723.3	-50.0	0.39203
6	1040	23.5	0.56753	1047.1	-50.0	0.56752
7	1040	22.9	0.56899	1049.8	-50.0	0.56899
8	1040	25.0	0.5639	1040.4	-50.0	0.56389
9	1008	24.0	0.54889	1012.7	-50.0	0.54888

Table 3: Overview of the temperatures and pressures used for the ADM-Aeolus geometry and wavelength to ensure the y-parameter value matches with the VU case.

.

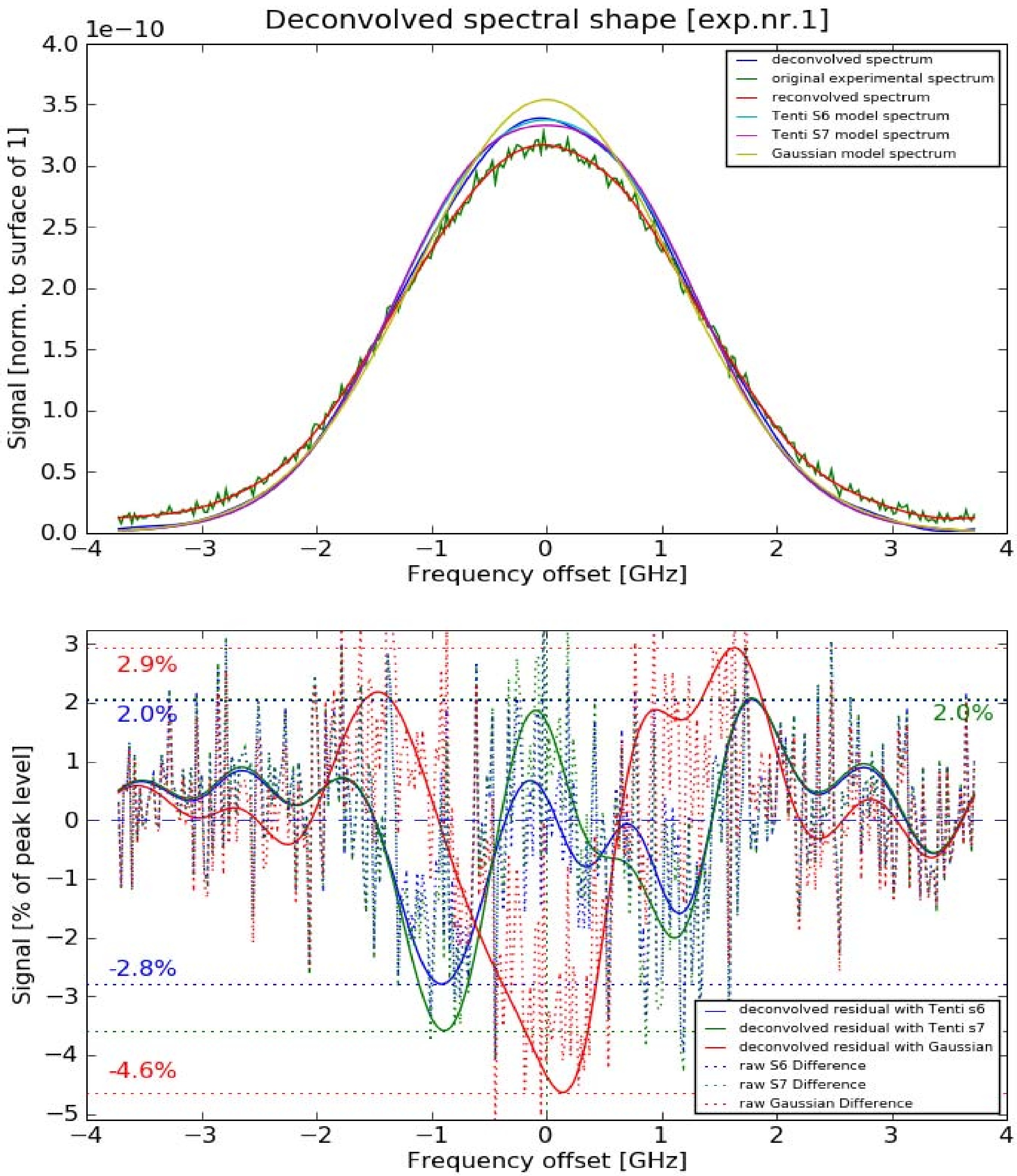

Figure 10: Deconvolution and residual calculation for experiment number 1 (pressure 300 hPa)

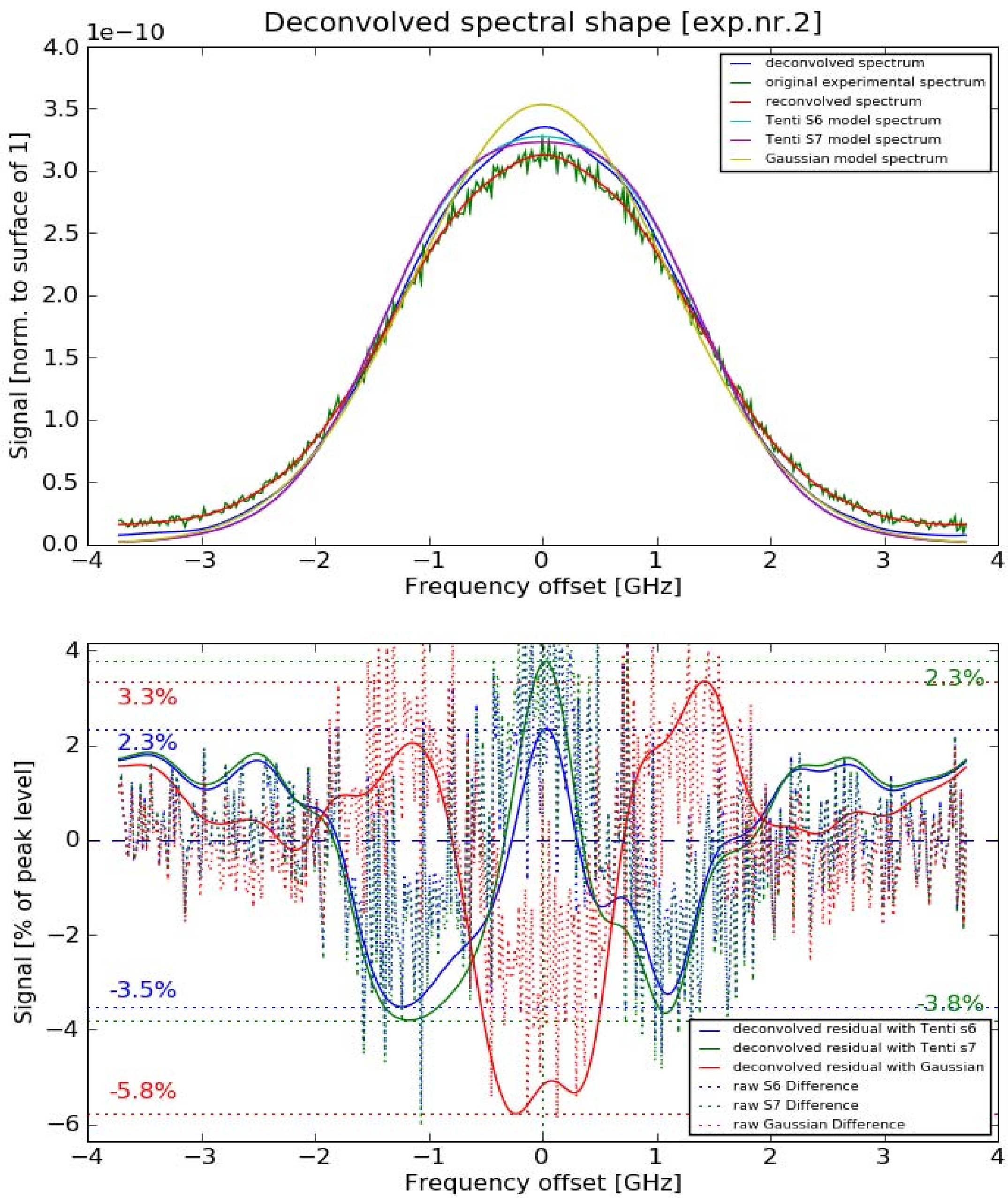

Figure 11: Deconvolution and residual calculation for experiment number 2 (pressure 503 hPa)

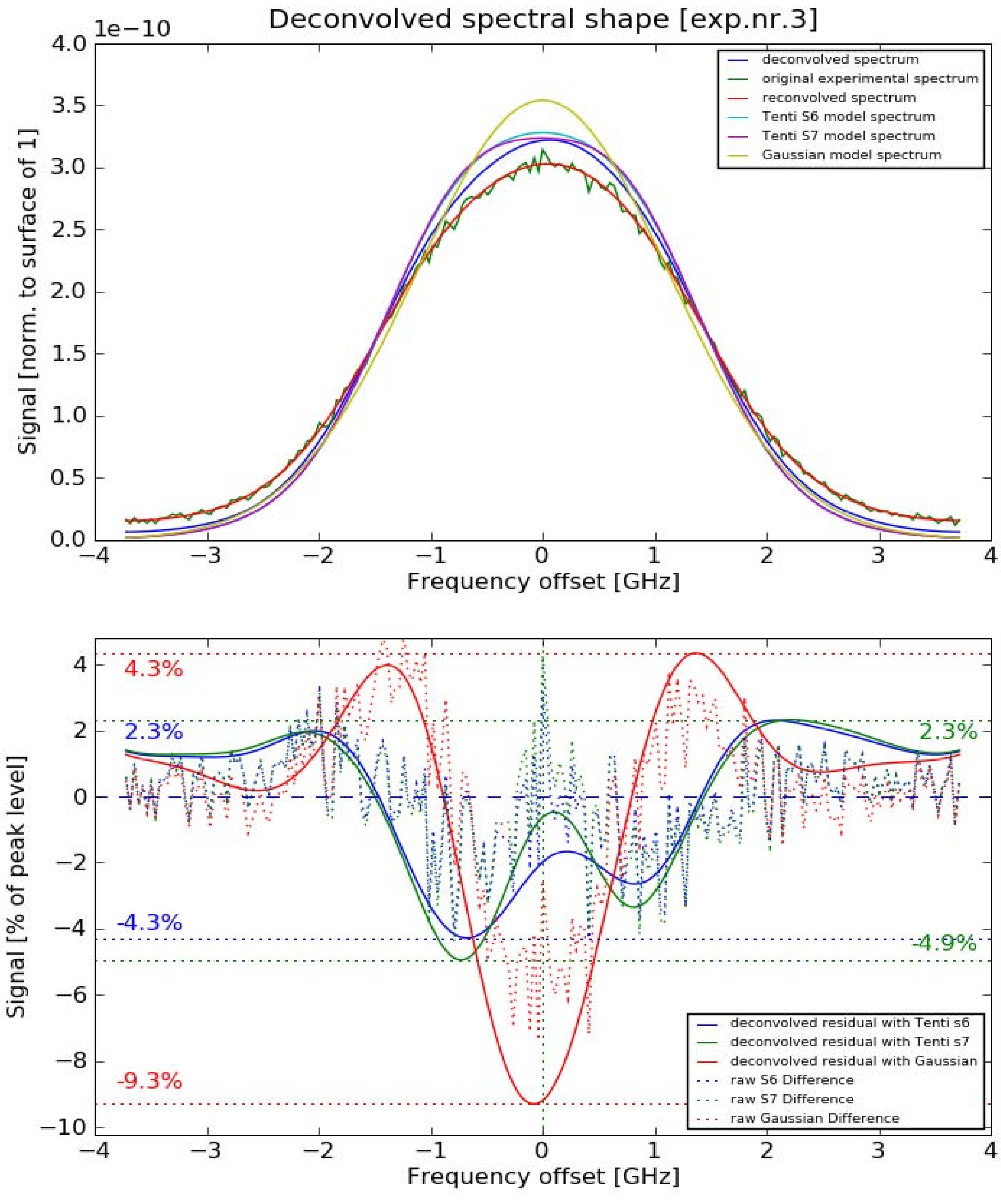

Figure 12: Deconvolution and residual calculation for experiment number 3 (pressure 504 hPa)

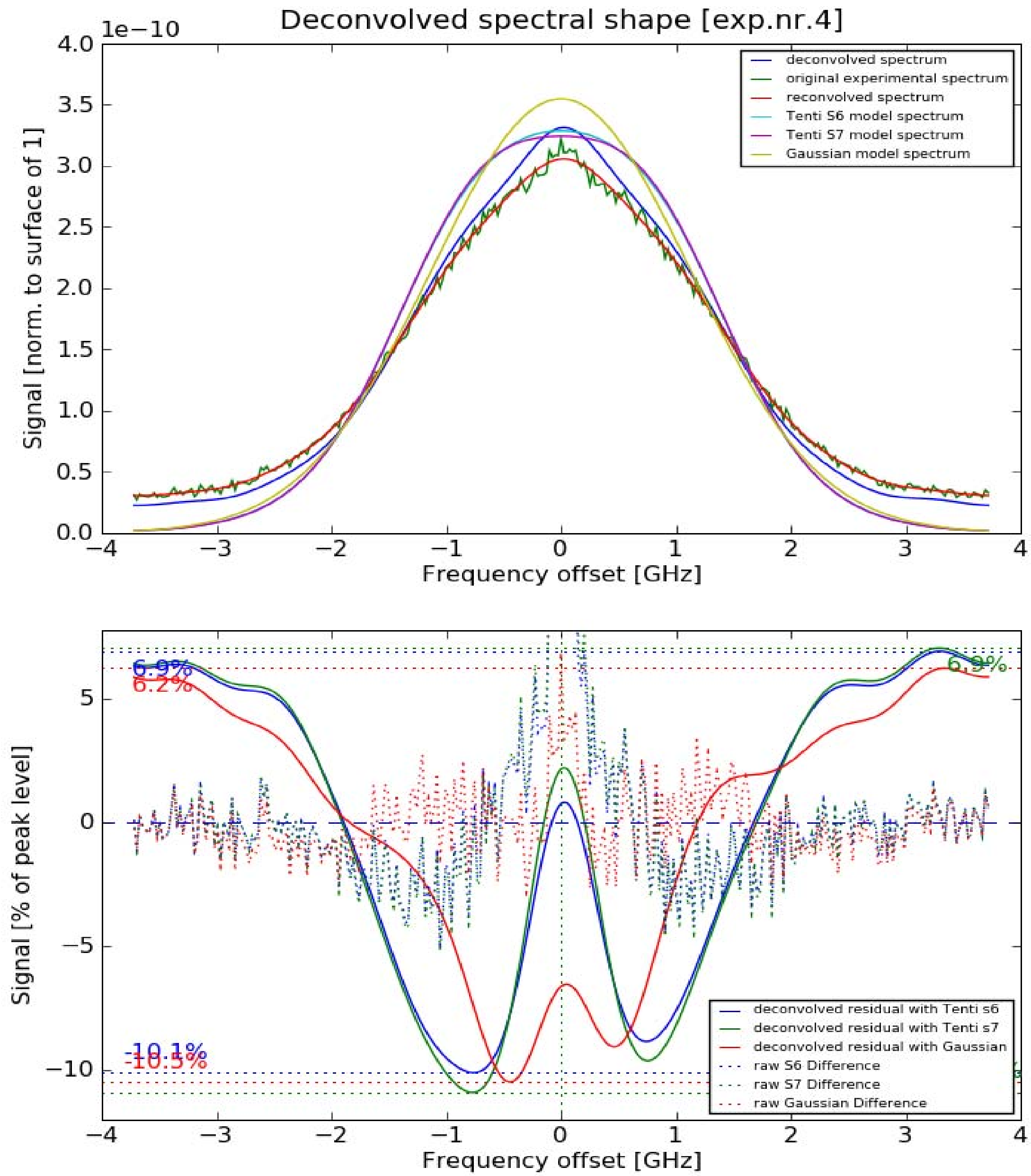

Figure13: Deconvolution and residual calculation for experiment number 4 (pressure 500 hPa). Note that this experiment clearly suffered from some Mie contamination.

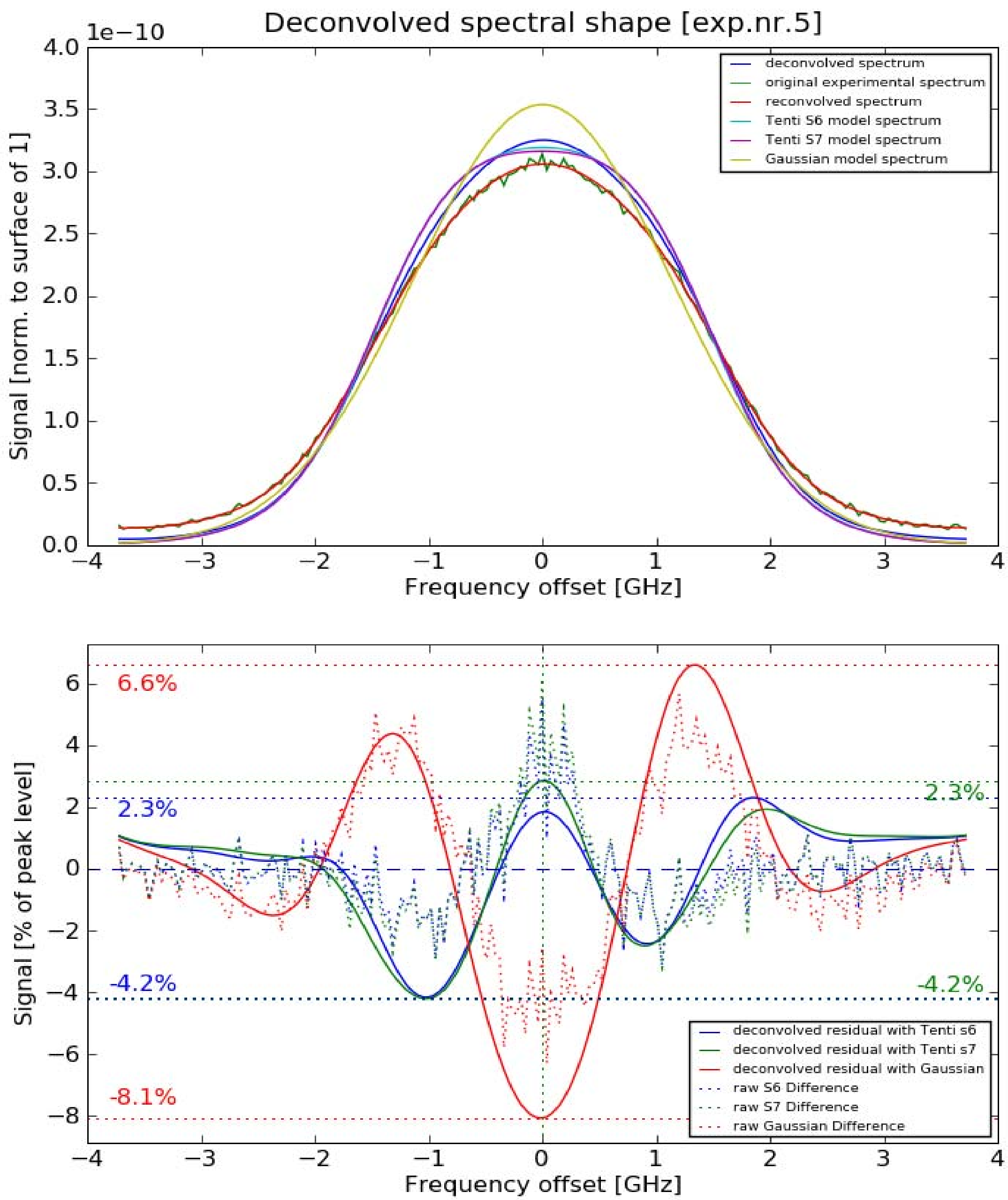

Figure 14: Deconvolution and residual calculation for experiment number 5 (pressure 725 hPa)

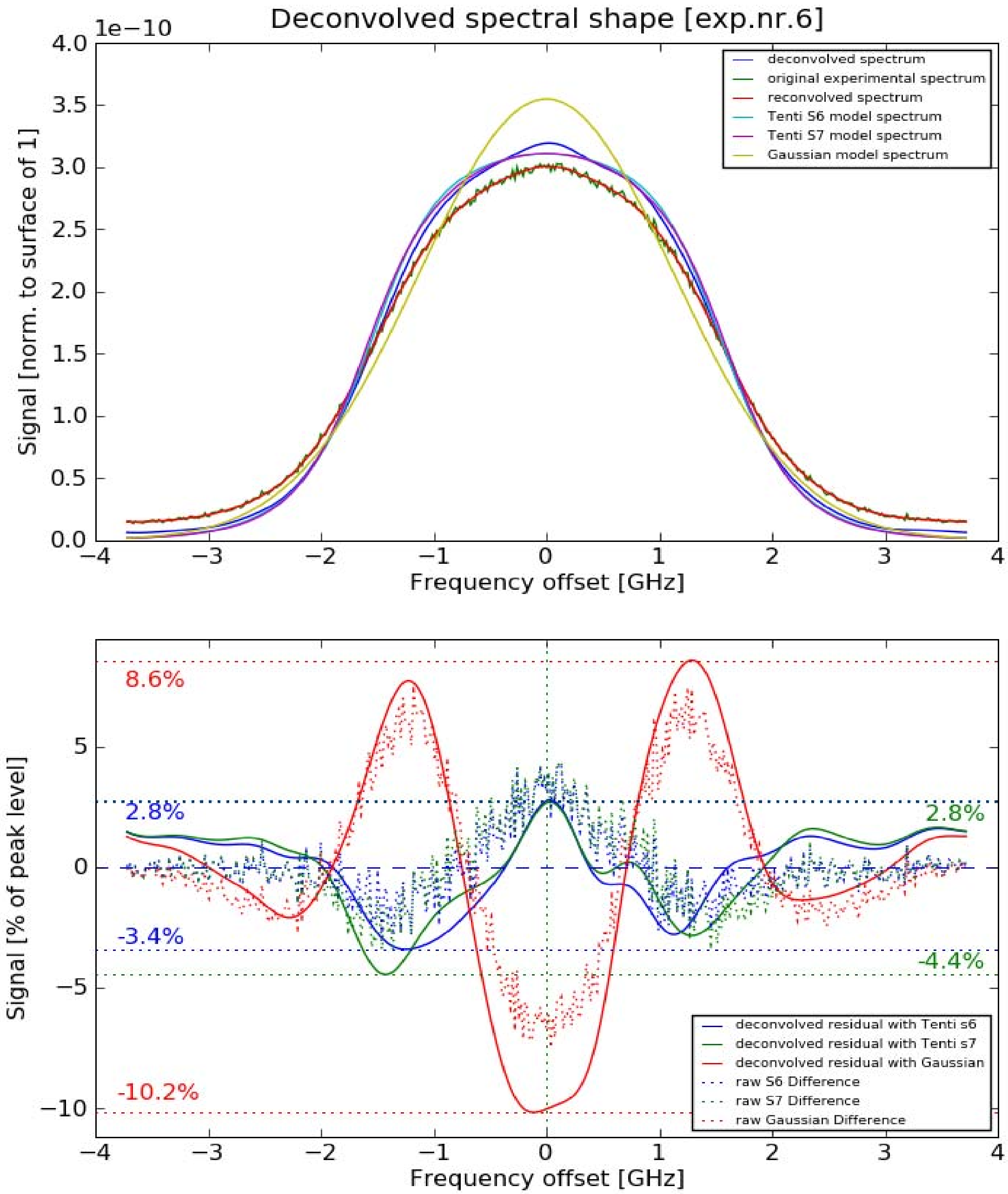

Figure 15: Deconvolution and residual calculation for experiment number 6 (pressure 1040 hPa)

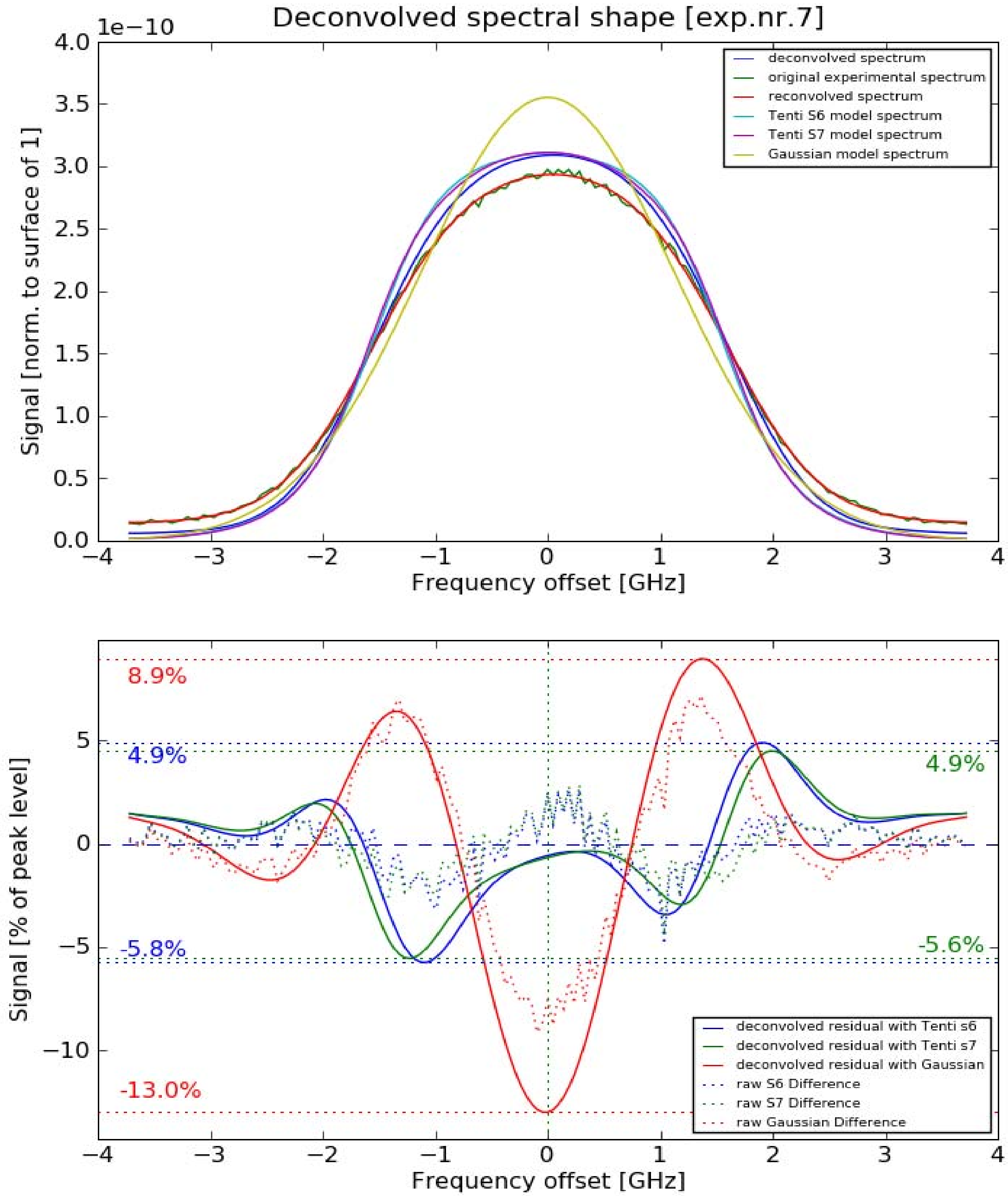

Figure 16: Deconvolution and residual calculation for experiment number 7 (pressure 1040 hPa)

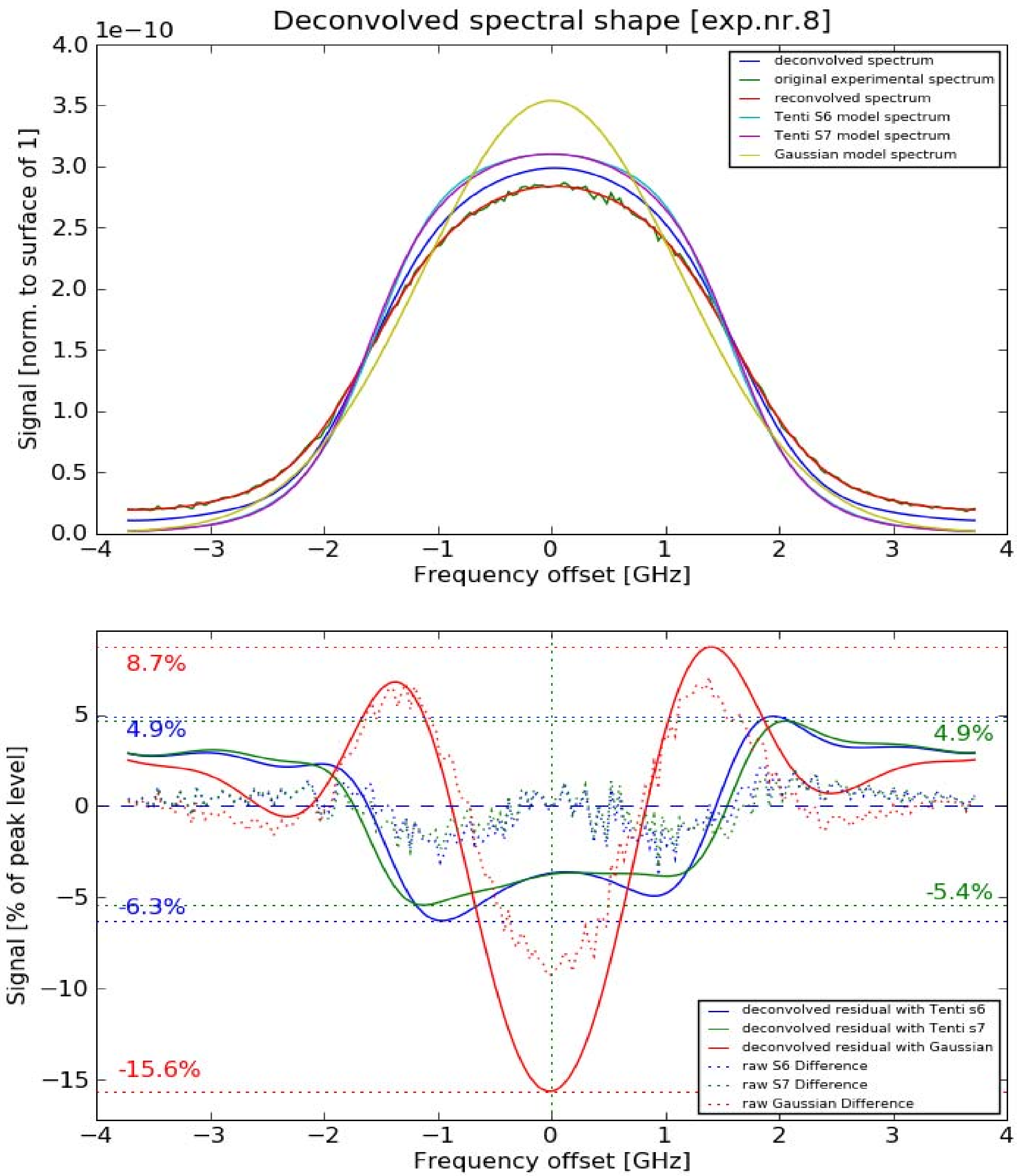

Figure 17: Deconvolution and residual calculation for experiment number 8 (pressure 1040 hPa)

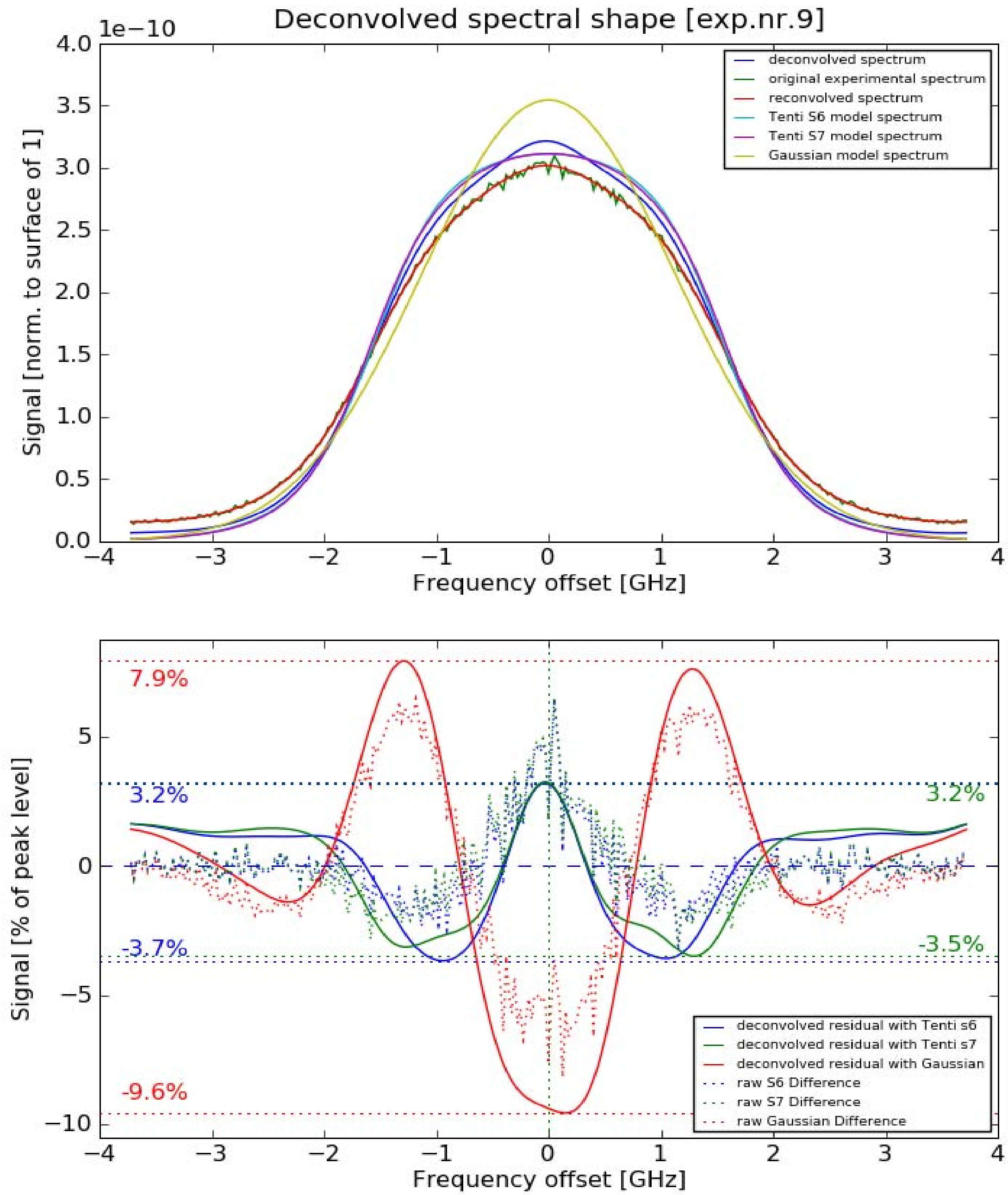

Figure 18: Deconvolution and residual calculation for experiment number 9 (pressure 1008 hPa)

- Step n: then the transmission function for the both Fabry-Pérot spectrometers of ADM-Aeolus is calculated (as described in section 2).
- Step o: finally a loop over a range of LOS wind values between -100 and 100 m/s in steps of 10 m/s was performed and for each wind velocity the LOS wind error was estimated by executing steps p to t. This loop is indicated by the box in the flow diagram in figure 9.
- Step p: the theoretical and the perturbed ADM-Aeolus spectra determined in step m are then shifted in frequency to reflect the Doppler shift for the current wind. Figure 19 shows an example of such shifted spectra.
- Step q: for each Fabry-Pérot spectrometer of ADM-Aeolus the signal is calculated by applying the transmission function determined in step n with the Doppler shifted perturbed spectrum determined in step p. From this the response R is calculated as is detailed in section 6 below. Figure 20 shows an example of the responses found for experiment 9.
- Step r: the response (as function of LOS wind) derived from the theoretical spectrum is then numerically inverted to yield a function of LOS wind (as function of response)
- Step s: now the response determined from the perturbed spectrum (calculated in step q) is inverted back to wind again, using the inverted response (calculated in step r).
- Step t: finally the perturbed LOS wind found in step s is compared to the input LOS wind assumed in step o. The difference should give an idea how the ADM-Aeolus system responds to deviations in the spectral shape similar to the residuals that have been observed in the VU experiments.

6 Relating residual errors in the spectrum to wind deviations

Next, the LOS wind is taken into account by shifting the ADM-Aeolus spectral response by the Doppler shift, using:

$$\delta\lambda = \frac{2\mathrm{v}_{LOS}\lambda}{c}$$

in which $\delta\lambda$ is the wavelength shift, and ν_{LOS} the LOS wind speed. The factor of 2 is caused by the backscattering geometry. This is done for both the unperturbed theoretical spectra, and for the spectra perturbed by the above calculated residuals. An example of these shifted spectra is shown in Figure 19.

Note that due to the rescaling and shifting it can occur that a part of the spectrum needed in the following transmission calculation is missing. In those cases the signal is just taken to be zero for these missing parts (which are usually at some distance of the centre of the spectral peak).

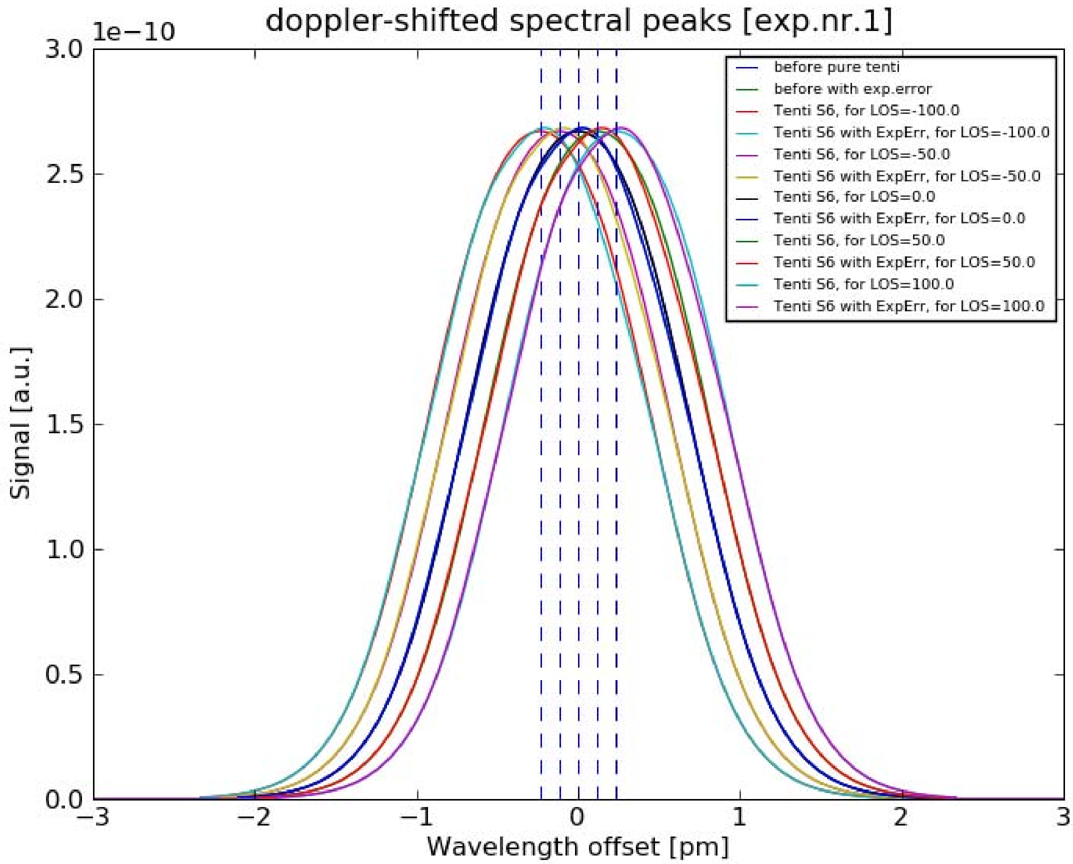

Figure 19: Spectra shifted by the Doppler effect, and used as input to the LOS error calculation.

The transmission found for both FP channels is then applied to the spectral shape derived in section 4 above, and this results in 2 signals, A and B. From this the response R is calculated using:

$$R = \frac{A - B}{A + B}$$

The responses have been calculated for each of the discussed 9 experiments, for the 3 theoretical models, and for a range of LOS wind velocities between -100 and 100 m/s.
The result is illustrated by Figure 20. The upper panel gives the calculated response against the assumed LOS wind. Because the curves are so close to each other, also the differences between the perturbed and unperturbed responses, and the derivative to the LOS wind has been plotted in the middle and lower panel.

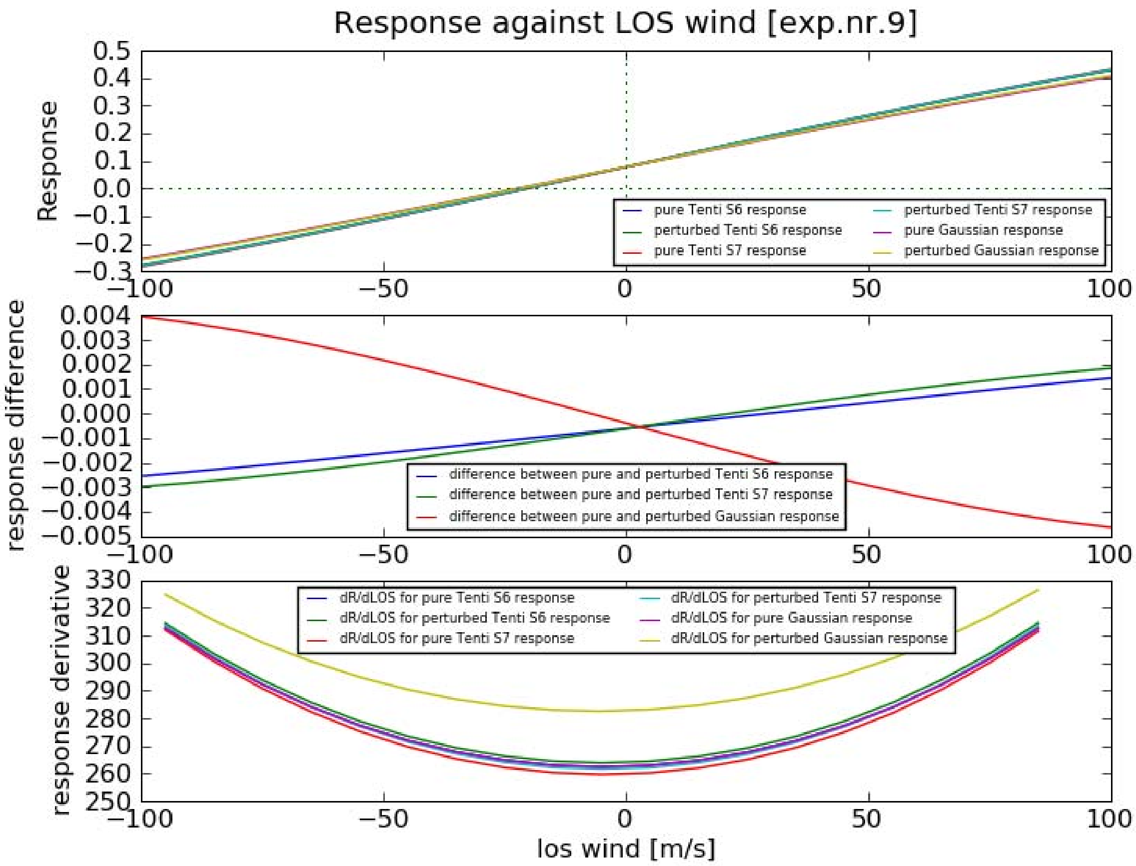

Figure 20: Response curves found for different LOS wind speeds, after perturbing the spectra with the

Finally, a simplified wind retrieval needs to be done. For this, the perturbed spectral shape (model + rescaled residual) was taken as truth. This perturbed response is then “inverted” to LOS wind again, using the response calculated by the unperturbed theoretical spectrum. The resulting error compared to the true LOS wind then gives an idea how the deformation of the spectrum, as observed by the VU experiments, will translate to an error in LOS wind. The results of this final step are given in Figures 21 to 29.

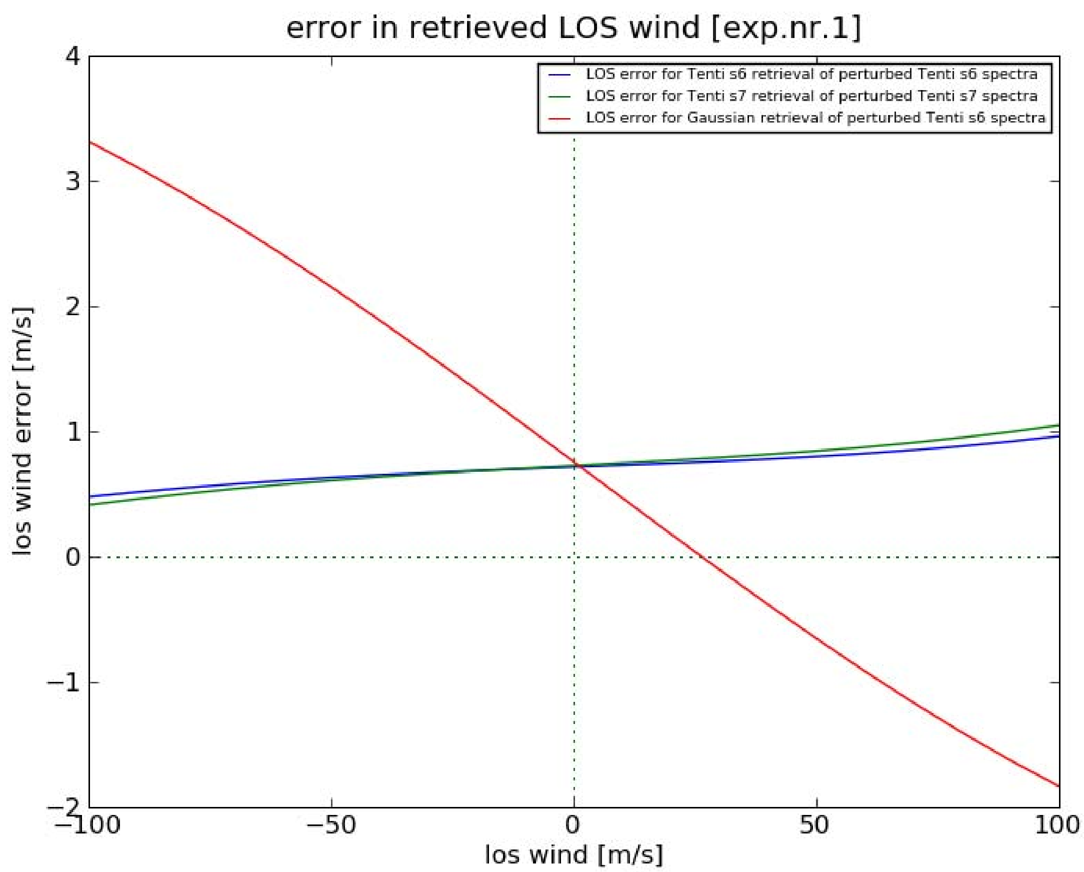

Figure 21: LOS wind error calculated from the residuals from experiment 1 (pressure 300 hPa).

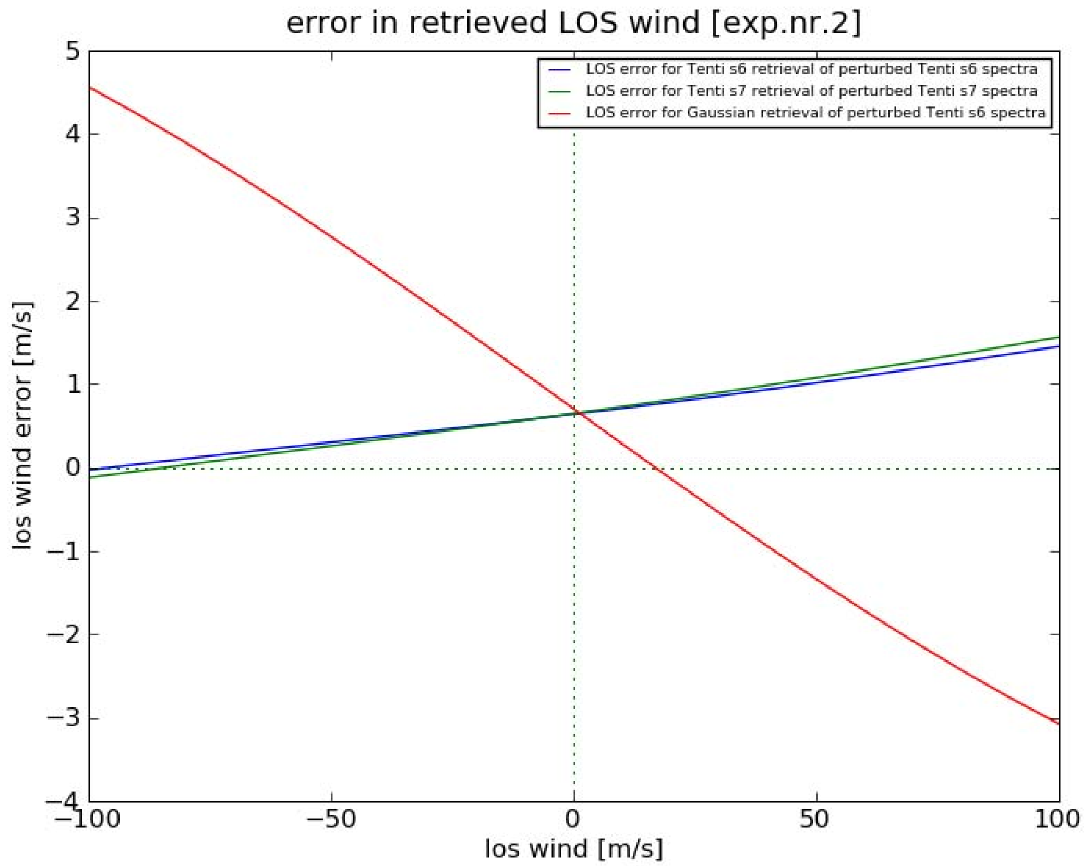

Figure 22: LOS wind error calculated from the residuals from experiment 2 (pressure 503 hPa).

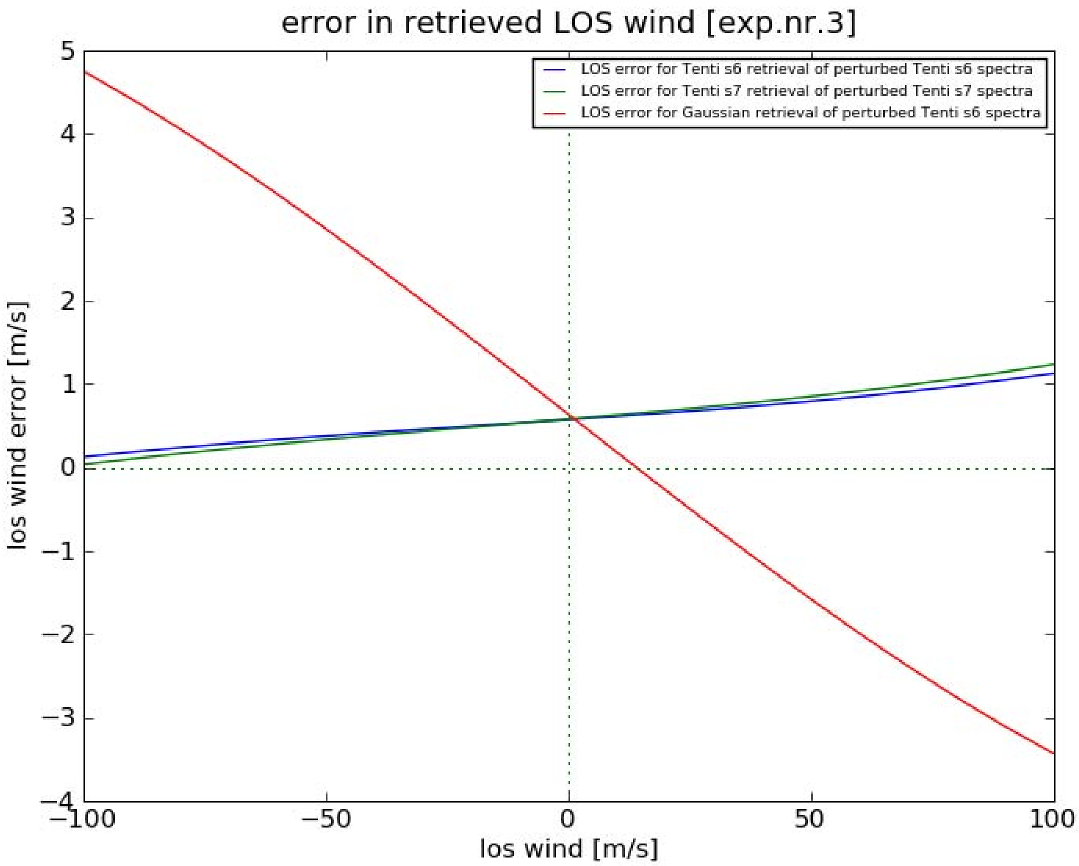

Figure 23: LOS wind error calculated from the residuals from experiment 3 (pressure 504 hPa).

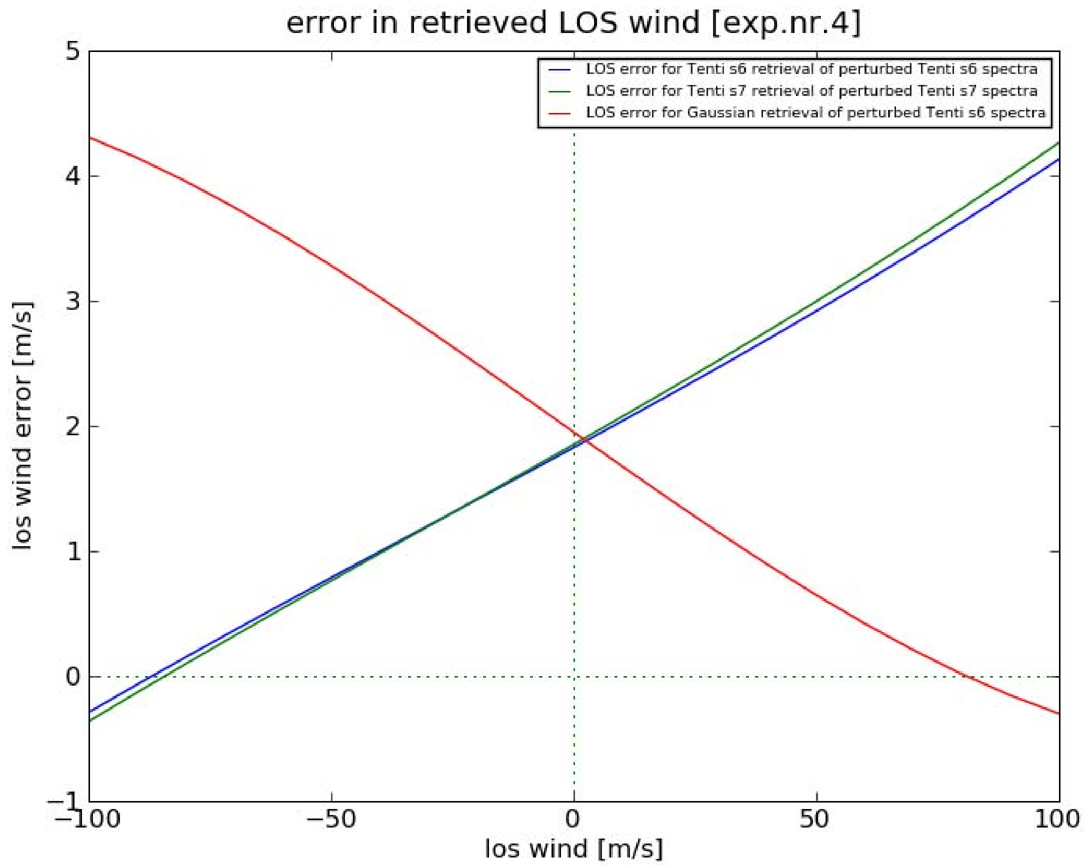

Figure 24: LOS wind error calculated from the residuals from experiment 4 (pressure 500 hPa). Note that this experiment clearly suffered from some Mie contamination.

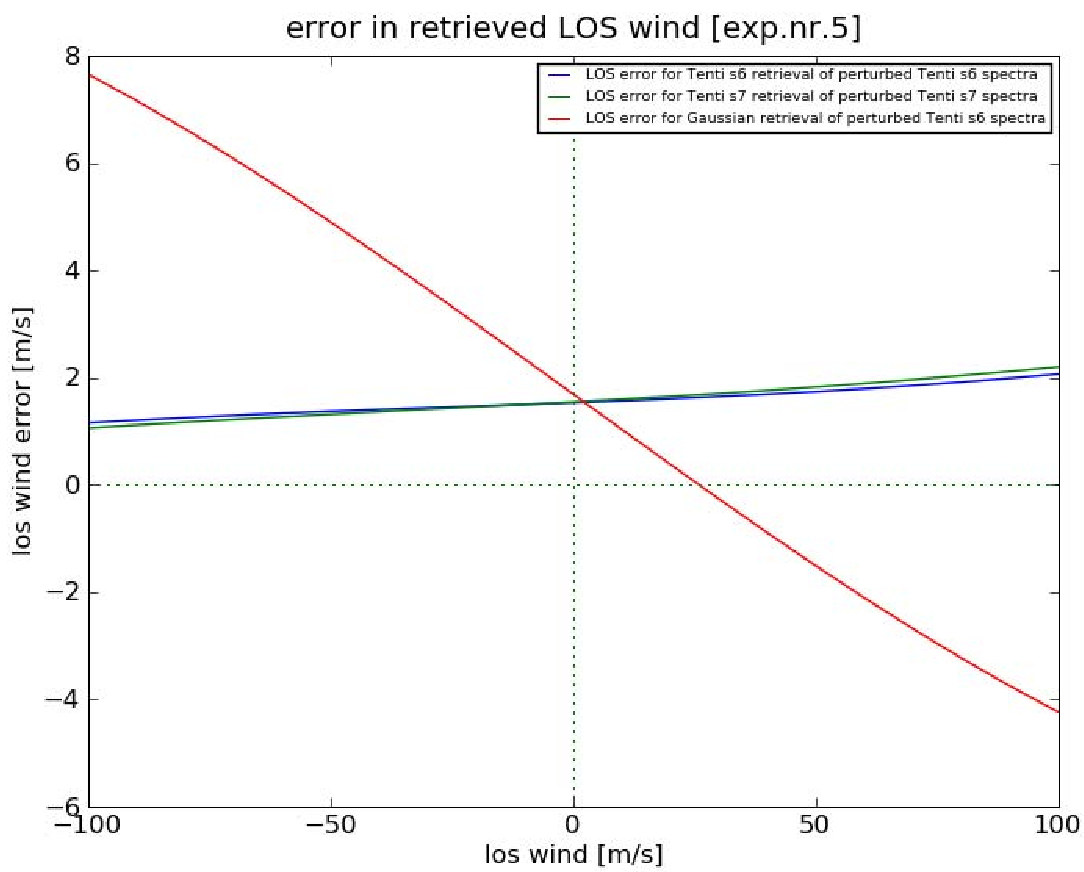

Figure 25: LOS wind error calculated from the residuals from experiment 5 (pressure 725 hPa).

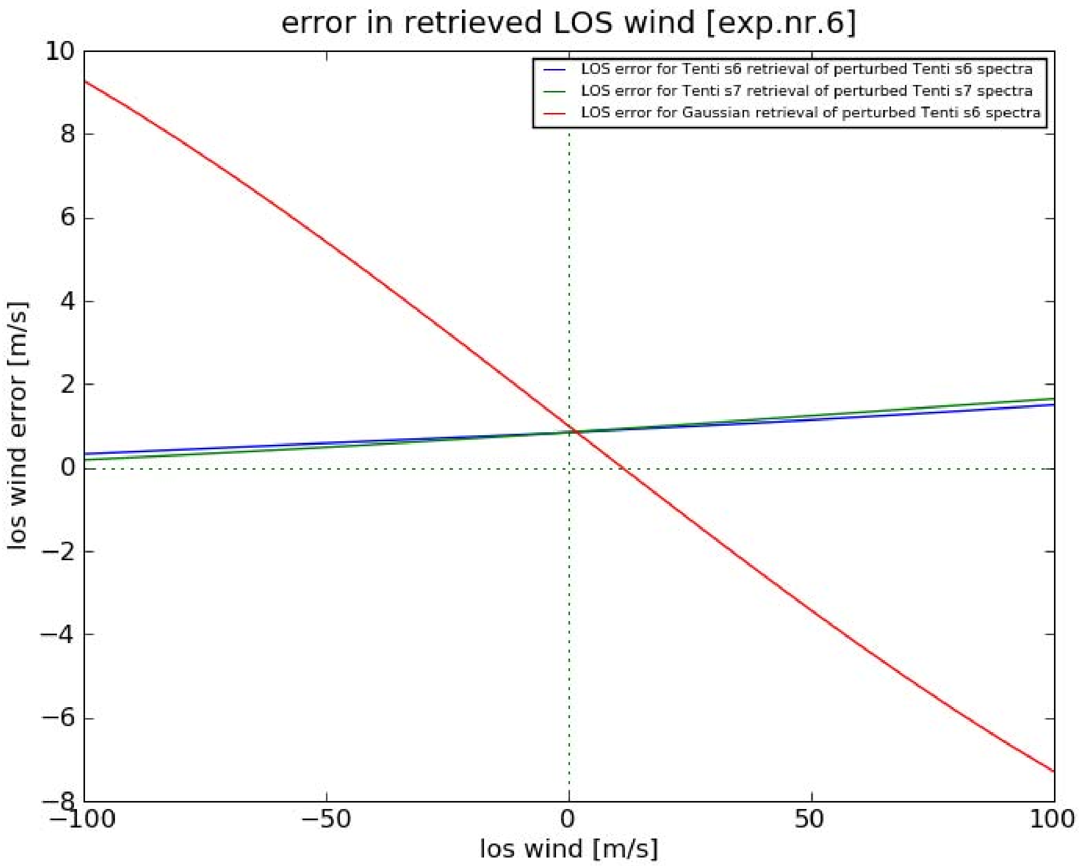

Figure 26: LOS wind error calculated from the residuals from experiment 6 (pressure 1040 hPa).

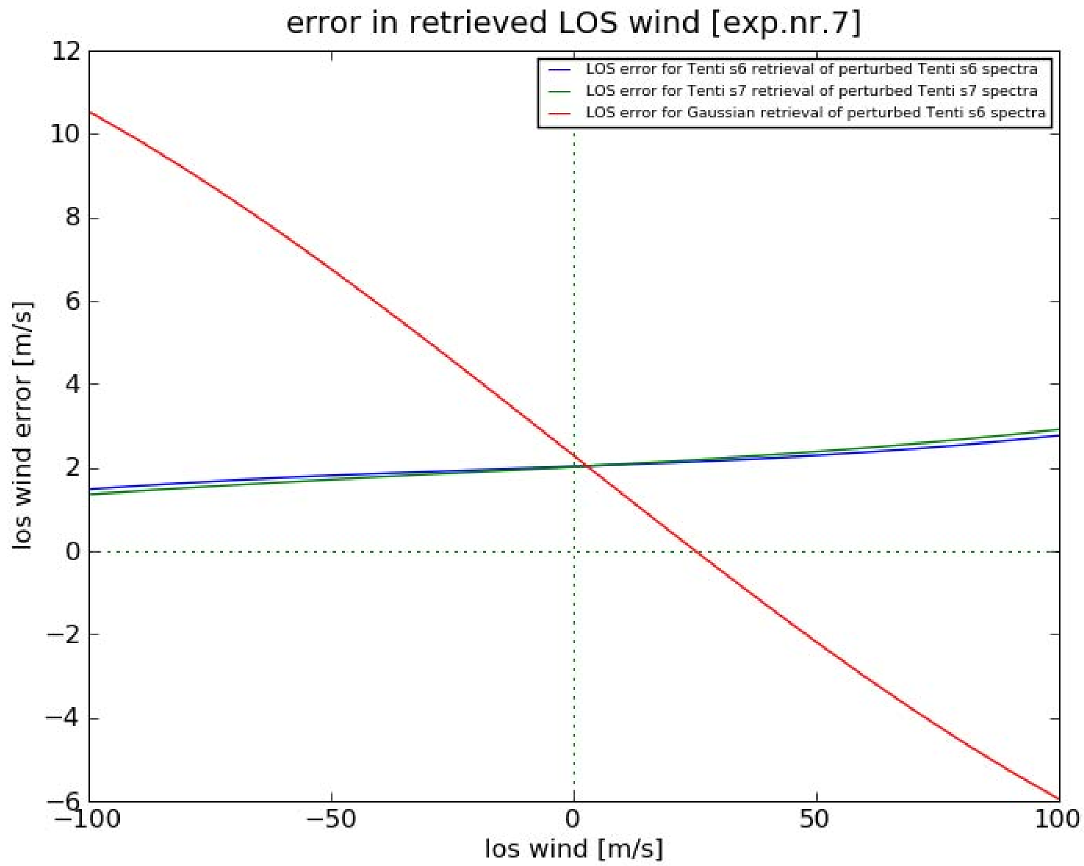

Figure 27: LOS wind error calculated from the residuals from experiment 7 (pressure 1040 hPa).

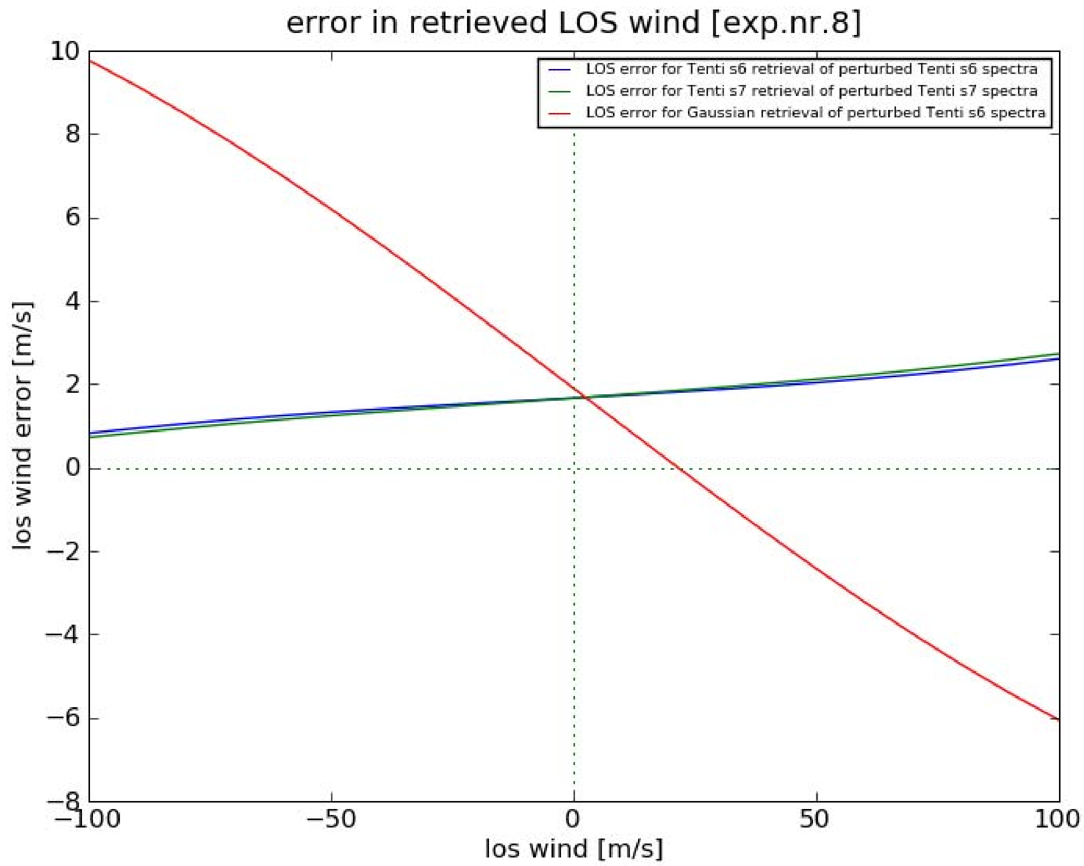

Figure 28: LOS wind error calculated from the residuals from experiment 8 (pressure 1040 hPa).

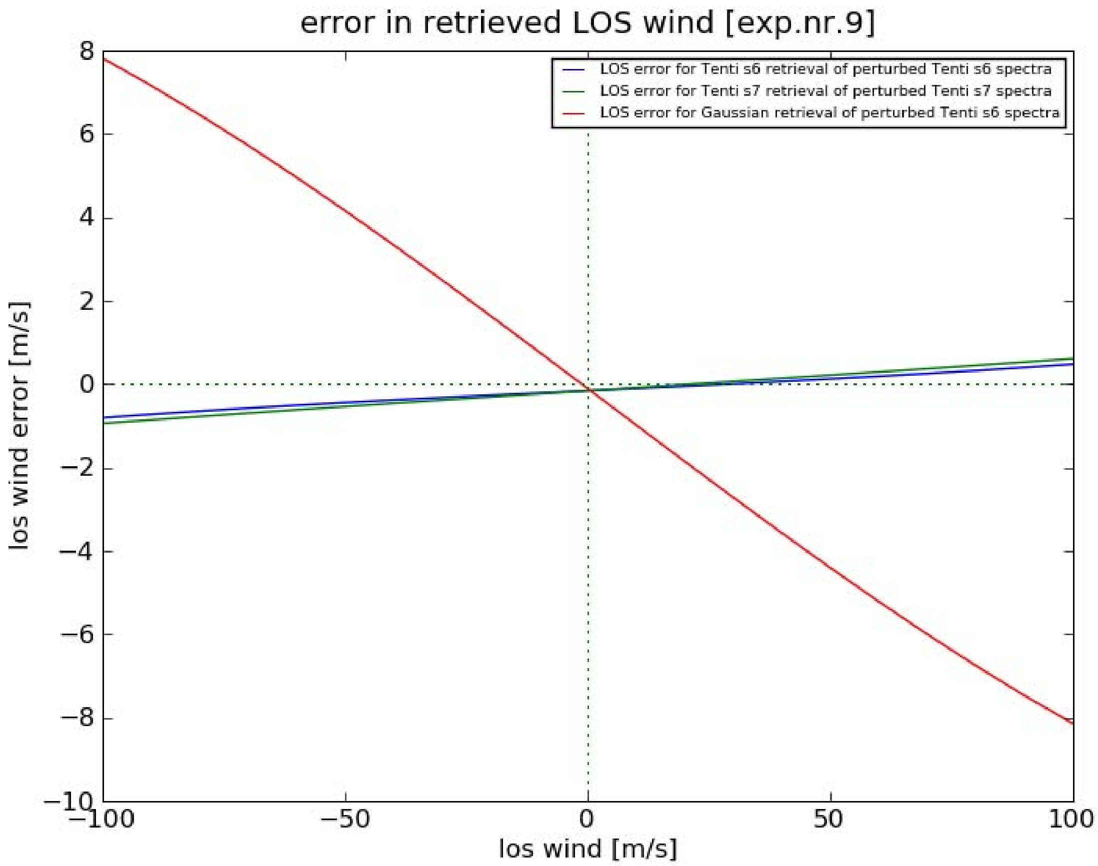

Figure 29: LOS wind error calculated from the residuals from experiment 9 (pressure 1008 hPa).

Clearly the error in LOS wind is much more sensitive to changes in the spectral shape than the responses are.
The Gaussian results are fairly close to the ones reported in the ILIAD study [R3], although ILIAD only report 2 LOS wind results. ILIAD reports LOS wind deviations in the order of 8 m/s for large input wind (LOS wind = 110 m/s) at the highest pressures (1000 hPa), and 1 m/s for moderate input winds (LOS wind – 13 m.s) ([R3], chapter 7, figures 7.10 and 7.11).

From results in Figure 21-29, it can be seen that the LOS wind error in most cases seems to have a significant constant offset and (on top) a small dependency on the input LOS wind. The only exception seems to be experiment 4, from which the LOS wind error shows a very strong dependency on input LOS wind. This is probably related to the deconvolution problem for that case, presumably due to Mie contamination.
It is also noticeable that for experiment 9 (Figure 29), there seems to be almost no offset in the error curve. This could be related to the very symmetric shape of the residual for this case.

The asymmetry for each experiment has been defined as follows:

$$asymmetry = \frac{1}{N}\sum_{i=1}^{N} abs(residual[i] - residual[N-i+1])$$

where N is the number of measurement points along the curve.
Note that this definition differs from the one in section 2.7 of TN3p1, whose description seems to be incomplete, and misses a summation or integral.

The calculated LOS wind errors in the Aeolus wind retrieval, when using the Tenti or Gaussian model line shapes in stead of the measured line shapes (Tenti model + measurement residual) are summarized in Table 4.

Exp.	Tenti S6			Tenti S7			Gaussian		
	Asymm. in residual	LOS wind error offset [m/s]	LOS wind error slope	Asymm. in residual	LOS wind error offset [m/s]	LOS wind error slope	Asymm. in residual	LOS wind error offset [m/s]	LOS wind error slope
1	0.754	0.715	0.0024	0.764	0.726	0.0032	0.719	0.749	-0.0257
2	0.530	0.666	0.0074	0.537	0.675	0.0084	0.491	0.719	-0.0382
3	0.648	0.593	0.0050	0.657	0.599	0.0060	0.601	0.643	-0.0409
4	1.325	1.861	0.0221	1.343	1.888	0.0231	1.228	1.970	-0.0230
5	1.069	1.563	0.0045	1.080	1.579	0.0057	0.965	1.696	-0.0594
6	0.621	0.868	0.0059	0.620	0.870	0.0073	0.543	0.994	-0.0828
7	1.451	2.058	0.0065	1.450	2.058	0.0078	1.270	2.290	-0.0824
8	1.195	1.684	0.0089	1.195	1.685	0.0100	1.047	1.880	-0.0791
9	0.211	-0.162	0.0064	0.211	-0.164	0.0078	0.185	-0.129	-0.0798

Table 4: Overview of the LOS wind error properties found for the 9 experiments.

7 Conclusions and recommendations

As is shown above, small uncertainties in the knowledge of the spectral shape of the Rayleigh-Brillouin backscattered signal are of importance to ESA's lidar missions. For the ADM-Aeolus Doppler wind lidar mission in particular such uncertainties may lead to errors in the retrieved LOS winds of a few m/s.

The Aeolus system requirements for the horizontally projected LOS winds are 2 m/s in the free troposphere (between 2 and 16 km altitude). Errors in the LOS wind retrieval on the order of m/s caused by an imperfect knowledge of the RBS line shape is therefore not acceptable (see [R2], table 4.1). Moreover, the type of errors reported here will be of a systematic nature (on each pressure level) and the requirement for the bias and so-called slope errors is even more stringent.

This error is related to (and partly proportional with) the actual wind velocity, so a part of the effect could be removed by calibrating the ADM-Aeolus instrument to the actual atmosphere. The difficulty will of course be the lack of in-situ measurements, so this calibration would need to be performed against a priori winds, pressures and temperatures produced by a Numerical Weather Prediction model. Mean global bias errors in NWP winds, pressures and temperatures are thought to be sufficiently low with respect to the systematic errors reported here to allow such calibration.

The question remains whether the Tenti model may be adapted/tuned to reduce the residuals with respect to the experiments, which present a more ideal solution. This will be discussed in more detail in the conclusions of the Final Report from this study.

The residuals between the modelled (Tenti) and "measured" (Tenti + measurement residuals) line shapes that were projected to the Aeolus configuration, showed that the uncertainties in the Tenti S6 RB model are generally much smaller than errors when assuming a purely Gaussian molecular motion PDF. When assuming that the "measured" (Tenti + residual) line shape is correct, most simulations show a bias of around 1 m/s and a response slope error of 0.2-0.9% in the Aeolus retrievals when using the Tenti S6 RBS line shapes (Table 4). Some of the uncertainty in the measurements may be related to Mie contamination and in case 4 we were not able to fit the residual well in the deconvolution approach adopted due to this. We thus excluded case 4 as unrepresentative.

From the presented results it is clear that there still is some room for improvement. In the applied procedure of translating the measured line shapes to the Aeolus configuration. In a number of cases the deconvoluted signal, using the measured FP instrument function, clearly amplifies the asymmetry in the residual as present in the VU experiments. This appears to result in the wind bias as seen from the different cases processed (Table 4). A better noise filtering may perhaps provide improved fits of the asymmetry in the residuals, and thus somewhat reduced biases. The slope error does not appear much affected by the amplified asymmetry.

Also the deconvolved residual seems to have an offset at the edges of the FSR (while it was expected to go to almost zero in the wings of the backscattered signal). This may be due to the fact that the data was not compensated for any arbitrary offsets (contrary to what was implemented in the rbs fitting program).

There has been some discussion on the validity of using a perfect Airy function to deconvolve the measured spectrum. The perfect Airy function does not fit the height of the different measured FP instrument modes very well. This is solved by rescaling each mode again to a top value of one. However, this rescaling combined with measurement noise might introduce small deviations in the shape of the transmission peak if many modes are accumulated to obtain a better SNR. Also a relative misalignment between the laser line and the Fabry-Perot cavity modes may influence the instrument function. An alternative approach would be to use the actual measured instrument function for this deconvolution, although this would introduce an additional noise term, which may deteriorate the results. This would also require the instrument function to be measured after each realignment.

The filtering Fast Fourier Transform (FFT) deconvolution approach used here was chosen because it is easy to implement with available standard tools. The approach provides a reasonable fit of the noisy and fitted residuals and a new approach may not yield very different results. Doing a Fourier transform and then applying a strong filter, basically seems equivalent to fitting to a sum of a few low-order polynomials (or any other set of basis functions). In both cases you need to truncate at some point, and this point will be rather arbitrary. This is true both for the FFT method and for a fitting method using any other basis. Wiener proposes an objective method where detection noise on top of the convoluted signal and instrument function is taken into account more rigorously [R5]. The method is based on an FFT basis and is well exploited in image processing [R4]. Although, the method closely resembles the approach taken here, it may well be able to correct some of the remaining artefacts noted above.

Note that the temperature and pressure dependency of the LOS wind errors have been studied before in the ILIAD study [R3]. The results from this study are consistent with the current results since the same LOS wind deviations, up to about 8 m/s where found at surface pressures and high input winds, when the wind retrieval was done using the Gaussian spectral shape.

Finally, since the L2B processing stage uses a look-up-table to invert the response of the FP spectrometer to wind, the table can be simply exchanged for a new one without much effort, as soon as a new and better model of the molecular motion spectrum would become available. Therefore efforts to improve the model can be continued until and even after the launch of ADM-Aeolus (validation from space).

References

[R1] ADM-Aeolus Science Report, ESA-SP 1311, April 2008.
(see: http://esamultimedia.esa.int/docs/SP-1311_ADM-Aeolus_FINAL_low-res.pdf)

[R2] Aeolus Level 1b Processor and End-to-End Simulator, End-to-End Simulator Detailed Processing Model (E2S DPM), ADM-MA-52-1801_E2S-DPM, v2.5, 27-Aug-2008

[R3] Loth, C., P.H. Flamant, A. Dabas, M.-L. Denneulin, A. Dolfi-Boutevre, A. Garnier and D. Rees, 2005: ILIAD Impact of Line Shape on Wind Measurements and Correction methods, ESA Contract No. 18334, 124p.

[R4] Rafael Gonzalez, Richard Woods, and Steven Eddins. Digital Image Processing Using Matlab. Prentice Hall, 2003.

[R5] N. Wiener, "The Extrapolation, Interpolation, and Smoothing of Stationary Time Series with Engineering Applications," Wiley, New York, 1949.